DIMITRI Algorithm Theoretical Basis Document [02]

Rayleigh Scattering Methodology for Vicarious Calibration

ARGANS

ESA contract: 4000106294

ARGANS Reference: 003-013: MO-SCI-ARG-TN-004b

Date: 28th May 2014

Version: 1.0

Authors

NAME	AFFILIATION	CONTACT
K. Barker	ARGANS Ltd, UK	kbarker@argans.co.uk
D. Marrable	ARGANS Ltd, UK	dmarrable@argans.co.uk
J. Hedley	ECS Ltd, UK	j.d.hedley@envirocs.com
C. Mazeran	Solvo, France	constant.mazeran@solvo.fr

Acknowledgements

The Siro modelling included in Figure 5 and Figure 6 were produced Jukka Kujanpää of the Finnish Meteorological Institute in the context of the ESA project 'GEO-HR' AO/1-7084/12/NL/AF, and are reproduced from Hedley *et al*. (2013).

TABLE OF CONTENTS

List of Figures

List of Tables

1 Introduction

1.1 Scope of this ATBD

Under ESA contract 4000106294 ("Earth Observation Multi-Mission Phase-E2 Operational Calibration: assessment of enhanced and new methodologies, technical procedures and system scenarios") DIMITRI v2.0 has been developed further and is now available as DIMITRI v3.0, in which new methodologies have been included, and the automated cloud screening improved.

An ATBD describes each of the new developments. The set of three ATBDs are:

[01] Automated Cloud Screening DIMITRI v3.0

[02] Absolute vicarious calibration over Rayleigh Scattering

[03] Vicarious calibration over Sunglint

This ATBD document is concerned with describing the Absolute calibration over Rayleigh Scattering over ocean. The document:

1) Describes the principles of this method;
2) Describes the implementation in DIMITRI v3.0 making use of LibradTran LUTs;
3) Presents results of implementation, sensitivity analyses and uncertainty estimations;
4) Describes the updates made to DIMITRI Human Machine Interface (HMI) and how the user can use this methodology.

1.2 DIMITRI

The Database for Imaging Multi-Spectral Instruments and Tools for Radiometric Intercomparison (DIMITRI) is an open-source software giving gives users the capability of long term monitoring of instruments for systematic biases and calibration drift, with a database of L1b top of atmosphere radiance and reflectances from a number of optical medium resolution sensors.

DIMITRI comes with a suite of tools for comparison of the L1b radiance and reflectance values originating from various medium resolution sensors over a number of radiometrically homogenous and stable sites (Table 1) at TOA level, within the 400nm – 4µm wavelength range. The date range currently available is 2002 to 2012. DIMITRI's interface enables radiometric intercomparisons based on user-selection of a reference sensor, against which other sensors are compared. DIMITRI contains site reflectance averages and standard deviation (and number of valid pixels in the defined region of interest, or ROI), viewing and solar geometries and auxiliary and meteorology information where available; this allows extractions of windspeed and direction, surface pressure, humidity and ozone concentration from MERIS products, and water vapour and ozone concentration from VGT-2 products. Each observation is automatically assessed for cloud

cover using a variety of different automated algorithms depending on the radiometric wavelengths available; manual cloud screening is also visually performed using product quicklooks to flag misclassified observations. DIMITRI also provides a platform for radiometric intercalibration from User defined matching parameters: geometric, temporal, cloud and ROI coverage. Other capabilities and functions include: product reader and data extraction routines, radiometric recalibration & bidirectional reflectance distribution function (BRDF) modelling, quicklook generation with ROI overlays, instrument spectral response comparison tool, VEGETATION simulation.

DIMITRI v2.0 has these two methodologies:

1. **Radiometric intercomparison based on angular and temporal matching**, based on the methodology of Bouvet (2006) and Bouvet et al (2007): Concomitant observations made under similar geometry and within a defined temporal window are intercompared at similar spectral bands.
2. **Radiometric intercomparison of VEGETATION simulated and actual observations**, making use of the ability to combine timeseries from all sensors into one "super sensor" and fitting a 3-parameter BRDF model to all observations to simulate TOA spectra of VEGETATION-2 (Bouvet, 2011).

DIMITRI v3.0 is evolved from DIMITRI v2.0 and has two additional methodologies and an improved automated cloud screening and cloud screening tool:

1. **Absolute vicarious calibration over Rayleigh Scattering,** based on the methodology of Hagolle et al (1999) and Vermote et al (1992) and utilising open ocean observations, to simulate molecular scattering (Rayleigh) in the visible and comparing against *the observed* ρ_{toa} to derive a calibration gain coefficient;
2. **Vicarious calibration over sunglint**, based on the methodology of Hagolle et al (2004); similar to Rayleigh scattering approach but accounting for sunglint reflectance contribution;
3. **Improved automated cloud screening,** exploiting the spatial homogeneity (smoothness) of validation sites when cloud free and applying a statistical approach utilising σ (ρ_{toa}) over a ROI, and defining variability thresholds, such as dependence on wavelength and surface type.

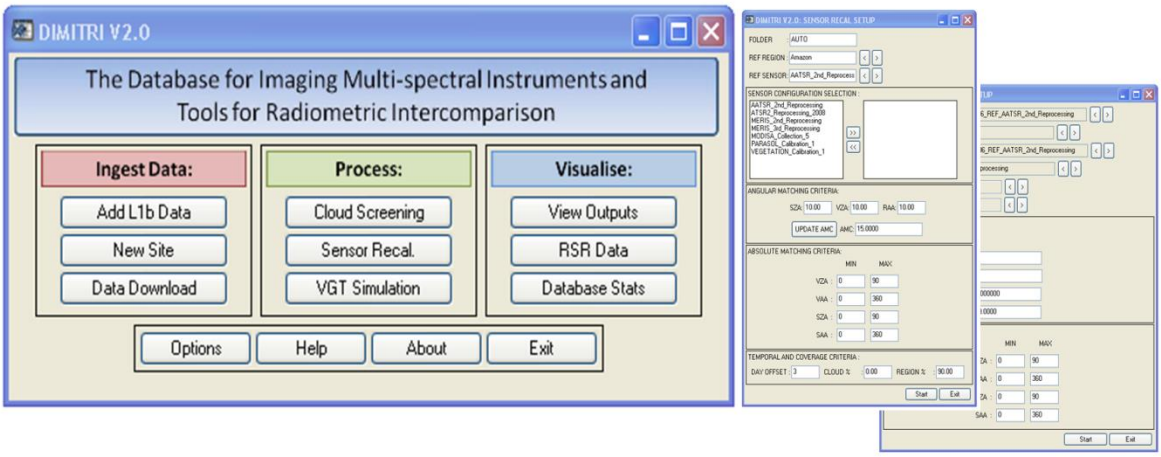

Figure 1: DIMITRI v2.0 screenshot

Table 1: Sensors and sites included in the DIMITRI v2.0 database

SENSOR	SUPPLIER
AATSR (Envisat)	ESA
MERIS, 2nd and 3rd reprocessing (Envisat)	ESA
ATSR-2 (ERS-2)	ESA
MODIS-A (Aqua)	NASA
POLDER-3 (Parasol)	CNES
VEGETATION-2 (SPOT5)	VITO

SITE	SITE TYPE
Salar de Uyuni, Bolivia	Salt lake
Libya-4, Libyan Desert	Desert
Dome-Concordia (Dome-C), Antarctica	Snow
Tuz Golu, Turkey	Salt Lake
Amazon Forest	Vegetation
BOUSSOLE, Mediterranean Sea	Marine
South Pacific Gyre (SPG)	Marine
Southern Indian Ocean (SIO)	Marine

DIMITRI_v2.0 and v3.0 are freely (without L1b data) available. DIMITRI_v2.0 is available following registration at www.argans.co.uk/dimitri. DIMITRI_v3.0 is a larger file (approx. 55GB) so is available upon request; ARGANS or ESA will make it available on an FTP server site.

2 Rayleigh Scattering Absolute Calibration

2.1 Overview

Rayleigh calibration methodologies utilise open ocean observations, in which the main component of the TOA signal is molecular scattering (Rayleigh) in the visible wavelengths; this scattering by molecules is well characterised and can be accurately computed. In these regions the TOA signal can be simulated using known models and the LibRadtran-generated LUTs. Other contributing components to the TOA signal include scattering by aerosols, the marine reflectance, specular reflection of the water surface (known as Fresnel reflectance), sun glint, gaseous absorption (e.g. ozone, water vapour, trace gases etc) and reflection from whitecaps.

The POLDER approach (Hagolle *et al*., 1999) aims to avoid the use of using an on-board calibration source by employing a calibration method over natural targets on the Earth; good results have been achieved this way for AVHRR/NOAA and METEOSAT (using molecular scattering over ocean for absolute calibration, high altitude clouds or ocean sunglint for interband calibration).

Absolute calibration methodologies such as Vermote *et al* (1992) and Hagolle *et al* (1999) aim to measure an absolute calibration coefficient, A^k. The Hagolle *et al* (1999) approach is that implemented in DIMITRI. This method, which builds on the Vermote *et al* (1992) approach, uses careful pixel selection to remove the contribution by white caps and sun glint through low wind speeds and pixels outside of the specular reflection respectively. Open ocean regions far away from coastal processes have been shown to have relatively stable marine reflectances (Fougnie *et al*., 2002); a range of realistic chlorophyll concentrations are used to estimate the marine reflectance using established models such as that of Morel (1998).

Following the detailed pixel criteria selection Vermote *et al* (1992) and Hagolle *et al* (1999) define the calibration coefficient A^k, computed using different aerosol models and chl-a concentrations, and then averaged over the sensor time series to provide one single calibration coefficient, for example as shown in Figure 2.

The Rayleigh contribution to the TOA signal, although large in the blue wavelengths, decreases considerably towards the Near Infrared (NIR); at these wavelengths the main contribution comes from the aerosol scattering (zero marine reflectance) and this can be used to provide an estimate of the aerosol properties. Using pre-defined aerosol models (Shettle and Fenn, 1979), the aerosol contribution in the NIR can be used to estimate the contribution in the visible wavelengths and thus allow simulation of the TOA reflectance. The Rayleigh method thus compares the model predicted reflectance to the observed reflectance to derive an estimation of the absolute calibration coefficient. This method cannot be applied to wavelengths above 700 nm since the Rayleigh scattering radiance becomes too small in the near infrared.

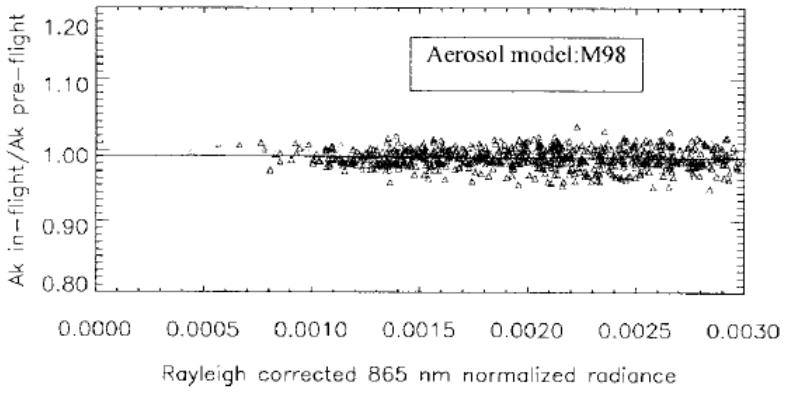

Figure 2: POLDER in-flight Rayleigh calibration coefficients from 100 orbits using the M98 Aerosol Model and a chl-a concentration of 0.035 mg.m^{-3}. From Hagolle *et al* (1999)

Calibration targets are selected in order to minimise the non-molecular radiance sources: a clear atmosphere is necessary, above a dark target (ocean, with a low wind speed to avoid foam). The main error sources for this calibration method are the water reflectance and the aerosol effects. In order to better define the water body contribution, the method is applied to oceanic zones where the chlorophyll concentration is stable. The aerosols are the most variable part of the atmospheric radiance and could induce errors in the absolute calibration. Very clear atmospheres are selected using a threshold on the radiance measured in a near infrared band (around 850 nm). Besides, for the selected pixels, the 865 nm radiance is used to determine the expected aerosol radiance in the calibrated band (Green and Chrien, 1999). For this extrapolation, it is necessary to rely on an aerosol type. The M98 (Maritime model with 98% of humidity) is generally used as the most likely. The Rayleigh based method is generally applied for large Field of View sensors. In this case, the method is applied as described in the paragraph above and the outputs are averaged on a significant number of images. The Rayleigh method can also be applied to small FOV sensors. It is mostly land sensors that occasionally acquire, on purpose, images over the open ocean. One way to get information on the aerosol model as well on the water contribution is to use simultaneous images of “ocean colour” sensors which provide at level 2 the relevant information: aerosol model and chlorophyll a amount.

Fougnie and Henry (2009) justify usage of Rayleigh scattering as the basis for calibration by the fact that molecular scattering may constitute as much as 90% of the TOA signal, for blue to red spectral bands. Climatology is used for marine reflectance, and cases too contaminated by aerosols are rejected, in contrast with vicarious radiometric calibrations using in-situ measurements in which the TOA signal is accurately computed using measurements of aerosol optical properties and water-leaving radiance. The advantage of the method using Rayleigh scattering is that the calibration is neither geographically nor geophysically limited, but is derived from a large set of oceanic sites, from both hemispheres and for a large set of conditions.

Hagolle *et al* (1999) comment that this methodology is an efficient method for absolute

calibration of optical instruments without the need for in-situ measurements.

The method provides calibration coefficients with a 3-4% uncertainty for spectral bands 490 nm and 565 nm. Hagolle *et al* (1999) point out that the use of oligotrophic waters is not the ideal case for the calibration of 443 channel due to high water-leaving radiances, and yet, it is not easy to find ocean zones away from the coasts with high and stable chlorophyll concentrations.

The use of in-situ measurements can therefore enhance results; Fougnie *et al*. (1999) have acquired in-situ data of water-leaving radiances, using SIMBADA instruments quasi-simultaneously with POLDER acquisitions.

2.2 Algorithm Description

A Rayleigh Scattering calibration methodology has been developed based on Vermote *et al*. (1992) and Hagolle *et al*. (1999) and is applicable to all DIMITRI_v2.0 sensors AATSR, ATSR2, MERIS, MODIS-A, PARASOL and VGT-2 (but only for BOUSSOLE; other marine targets are not available in DIMITRI). The following sections summarises the dataset, signal modelling and vicarious coefficient computation.

2.2.1 Oceanic sites

Rayleigh calibration is applicable on stable oceanic regions, with low concentration of phytoplankton and sediment in order to neglect the marine signal at 865 nm, and far from land to ensure a purely maritime aerosol model. Two regions in DIMITRI are candidates: South Pacific Gyre (SPG) and South Indian Ocean (SIO).

2.2.2 Data screening

Clear conditions must be chosen to avoid any signal contamination by clouds, haze or cloud shadows. As we shall see, a 0% cloud coverage at ROI level is mandatory for proper computation of the vicarious coefficients.

A low wind speed is required for ensuring no presence of whitecaps; typically it is limited to 5 m/s.

Small content of aerosol must be insured for avoiding any error propagation in the atmospheric path radiance. We follow Hagolle *et al*. (1999) by considering the Rayleigh corrected normalised radiance at 865 nm (directly related to aerosol amount):

$$R_{RC}(865) = (\rho_{TOA}(865) - \rho_R(865)) \cos\theta_s \quad (1)$$

The very stringent threshold at 865 nm of 0.002 also avoids using further data screening for sun glint.

2.2.3 Marine model

The DIMITRI marine model follows Morel and Maritorena (2001), which is an update of Morel (1988) used in Hagolle *et al*. (1999). It provides an estimate of irradiance reflectance at null depth, $R(0^-)$, from 350 to 700 nm, as a function of chlorophyll concentration and sun zenith angle. The water absorption coefficients of pure water are derived from Pope and Fry (2007) and Kou *et al*. (1993) and scattering coefficients from Table 1 of Smith and Baker (1981).

An excellent agreement is found between the original Morel and Maritorena (2001) model and DIMITRI implementation over the 400-700 nm spectral range, see Figure 2; discrepancy for wavelengths shorter than 400 nm, not considered in the vicarious calibration, are due to slight differences in input water coefficients.

Conversion from $R(0^-)$ to marine reflectance above sea surface is given by Morel and Gentili (1996):

$$\rho_w(\lambda) = \pi \frac{\Re}{Q} R(0^-) \quad (2)$$

Where:

$\Re$ is the term accounting for all the reflection and refraction effects, with averaged value of 0.5287 for moderate wind speed (see Appendix D of Morel and Gentili, 1996)

Q is the ratio of irradiance to radiance (at 0^-); without further details available in the Hagolle *et al*. (1999) methodology we consider here Q= π for isotropic distribution.

Note that there is no need for foam modelling since the vicarious calibration methodology only selects low wind speed modulus.

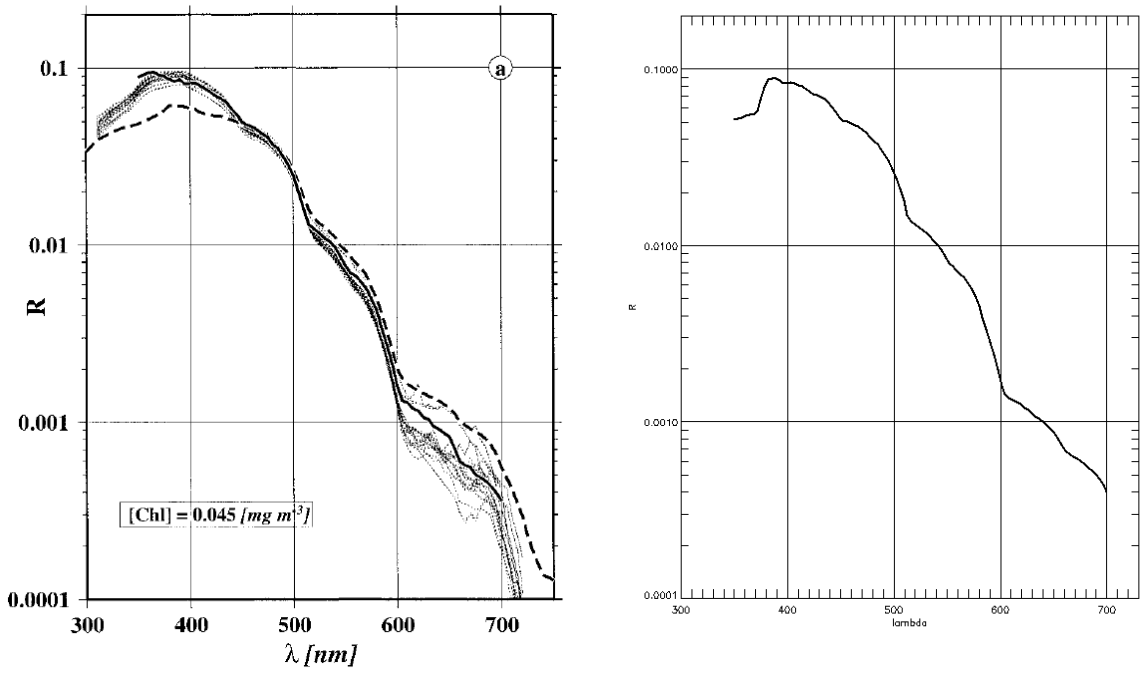

Figure 2: Comparison of irradiance reflectance spectrum between Morel and Maritorena (2001). *Left*: their figure 10a, solid thick line and *Right:* DIMITRI model (right) for a chlorophyll concentration of 0.045 mg/m^3.

2.2.4 Atmospheric model

The total TOA signal can be written as:

$$\rho_{TOA}(\lambda) = t_{gas}(\lambda)\left(\rho_{path}(\lambda) + t_{down}(\lambda) * t_{up}(\lambda) * \rho_w(\lambda) + T_{down}(\lambda) * T_{up}(\lambda)\rho_G\right) \quad (3)$$

Where:

t_{gas} is the transmittance (downward and upward) due to absorbing gas as O3, O2 and H2O

ρ_{path} is the atmospheric reflectance due to Rayleigh and aerosols and their multiple-scattering interaction

t_{down} and t_{up} are respectively the downward and upward total transmittance (i.e. direct + diffuse) due to Rayleigh and aerosol

ρ_w is the marine signal already described

T_{down} and T_{up} are the downward and upward direct transmittances

ρ_G is the sun glint reflectance at sea level.

Data selection in the Rayleigh calibration is such that:

- ρ_G is neglected
- ρ_w is neglected in the near-infrared (band 865 nm especially)

Rayleigh calibration coefficients are computed for all DIMITRI bands in the visible domain; we extend the original limit at 550 nm of Hagolle *et al*. (1999) up to 670 nm, as done more recently by Fougnie *et al*. (2012). Also the near-infrared 865 m band is used to estimate aerosol optical thickness (see next section). The methodology must not be applied to sensors having spectral bands in which there is significant water vapour absorption. For instance, for MERIS the only atmospheric gas impacting these bands is ozone, if we neglect residual water vapour absorption at 665 and 865 nm, as done for instance in the operational MERIS processing (MERIS DPM, 2011). Hence the gaseous transmittance is computed by Beer's law:

$$t_{gas}(\lambda) = t_{O_3}(\lambda) = e^{-\tau_{O_3}(\lambda) * O_3 * M} \quad (4)$$

Where:

O_3 is the ozone concentration of actual measurement

τ_{O_3} the ozone optical thickness at a standard concentration (already provided in DIMITRI auxiliary data)
M the air mass fraction.

The path reflectance and total transmittance are computed by radiative transfer simulations (see hereafter) for a set of aerosol models and optical thicknesses, and stored in Look-up tables (LUT). Aerosols models must be representative of the calibration zone; marine models of Shettle and Fenn (1974) are here chosen for several relative humidities. Other more complex models may also be used for sensitivity study.

Retrieval of aerosol optical thickness from knowledge of the path reflectance follows the standard approach in ocean colour, consisting of fitting the signal by a 2nd order polynomial in optical thickness, for every grid node of the simulation ($w_m, \theta_s, \theta_v, \Delta\varphi$ for wind modulus, sun zenith angle, view zenith angle and relative azimuth angle respectively); more particularly, the ratio of the path signal by the pure Rayleigh is used in fit as being found more robust (Antoine and Morel 1999):

$$\tau_a(\lambda) \rightarrow \left\{\frac{\rho_{path}}{\rho_R}\right\}(\lambda, \tau_a, w_m, \theta_s, \theta_v, \Delta\varphi) = XC_0 + XC_1\tau_a + XC_2(\tau_a)^2 \quad (5)$$

Where XC_i are the coefficients of the polynomial fit, defined for every wavelength, grid node and aerosol model.

Radiative transfer simulations are only tabulated for the unique standard atmospheric pressure, noted P_{std}. Because the actual measurements are under different pressures, P, generally systematically higher due to clear sky condition, a correction on ρ_{path} and $t_{down} * t_{up}$ is necessary. Here we follow here the MERIS pressure correction written in terms of:

$$\frac{\Delta P}{P_{std}} = \frac{(P - P_{std})}{P_{std}} \tag{6}$$

For ρ_{path}, Antoine and Morel (2011) proposes the following correction allowing to retrieve the exact signal within 0.5%

$$\rho_{path}(\lambda)_{|P} = \rho_{path}(\lambda)_{|P_{std}} * \left(1 + \frac{\Delta P}{P_{std}}\eta(\lambda)\right) \tag{7}$$

Where η is the contribution of molecules to total optical thickness:

$$\eta(\lambda) = \frac{\tau_R(\lambda)}{\tau_R(\lambda)+\tau_a(\lambda)} \tag{8}$$

Without this correction the error would be roughly similar as $\frac{\Delta P}{P_{std}}$ for low aerosol optical thickness, e.g. of 1% when $P = 1023$ hPa. It is worth noting that in the present work, the impact of pressure on computed ρ_{path} in the visible is lower, as we shall see in section 2.2.6, due to cancellation between combined use of NIR and visible bands; a correction is however still required to minimize errors in calibration coefficients towards the blue.

For the total transmittance, the MERIS correction for pressure (see MERIS DPM, 2011) relies on the Rayleigh contribution of $t_R = e^{-\frac{1}{2}\tau_R * M}$, hence:

$$t_{down}(\lambda) * t_{up}(\lambda)_{|P} = t_{down}(\lambda) * t_{up}(\lambda)_{|P_{std}} * e^{-\frac{1}{2}\tau_R * M\frac{\Delta P}{P_{std}}} \tag{9}$$

2.2.5 Calibration coefficient algorithm

The algorithm consists of following steps, repeated for all bands λ:

1. Given an aerosol model chosen by the user, retrieve the aerosol optical thickness at 865 nm by inversing the tabulated $\tau_a \rightarrow \left\{\frac{\rho_{path}}{\rho_R}\right\}$ relationships. Because the pressure correction needs knowledge of τ_a, an iterative scheme is implemented, starting with $\tau_{865} = 0.05$ and

converging in 3 loops:

1.1. Correct $\rho_{TOA}(865)$at standard pressure

$$\rho_{TOA}(865)_{|P_{std}} = \rho_{TOA}(865)_{|P} * \left(1 - \frac{\Delta P}{P_{std}} \frac{\tau_R(865)}{\tau_R(865)+\tau_{865}}\right) \quad (10)$$

1.2. Inverse optical thickness (2nd order polynomial inversion)

$$\tau_{865} \xleftarrow{LUT\ aer} \frac{\rho_{TOA}(865)_{|P_{std}}}{\rho_R(865,w_m,\theta_s,\theta_v,\Delta\varphi)} \quad (11)$$

Only pixels allowing a positive solution are kept.

2. Propagate aerosol optical thickness through tabulated spectral dependence:

$$\tau_{865} \xrightarrow{LUT\ aer} \tau_\lambda = \tau_{865} * c_\lambda \quad (12)$$

3. Compute total path radiance (Rayleigh + aerosol) and correct for pressure:

$$\tau_\lambda \xrightarrow{LUT\ aer} \rho_{path}(\lambda)_{|P_{std}} = \left\{\frac{\rho_{path}}{\rho_R}\right\}(\lambda,\tau_\lambda,w_m,\theta_s,\theta_v,\Delta\varphi) * \rho_R(\lambda,w_m,\theta_s,\theta_v,\Delta\varphi) \quad (13)$$

$$\rho_{path}(\lambda)_{|P} = \rho_{path}(\lambda)_{|P_{std}} * \left(1 + \frac{\Delta P}{P_{std}}\eta(\lambda)\right) \quad (14)$$

4. Compute downward and upward total transmittances (direct + diffuse), accounting for Rayleigh and aerosol, and correct for pressure:

$$\tau_\lambda \xrightarrow{LUT\ aer} t_{down}(\lambda)_{|P_{std}} = \{t_{down}\}(\lambda,\tau_\lambda,w_m,\theta_s) \quad (15)$$

$$\tau_\lambda \xrightarrow{LUT\ aer} t_{up}(\lambda)_{|P_{std}} = \{t_{up}\}(\lambda,\tau_\lambda,\theta_v) \quad (16)$$

$$t_{down}(\lambda) * t_{up}(\lambda)_{|P} = t_{down}(\lambda) * t_{up}(\lambda)_{|P_{std}} * e^{-\frac{1}{2}\tau_R * M \frac{\Delta P}{P_{std}}} \quad (17)$$

5. Given a chlorophyll concentration, compute marine reflectance following Morel and Maritorena (2001):

$$Chl, \theta_s \rightarrow \rho_w(\lambda) \quad (18)$$

6. Construct theoretical TOA signal by:

$$\rho_{TOA}^{theo}(\lambda) = \rho_{path}(\lambda)_{|P} + t_{down}(\lambda) * t_{up}(\lambda)_{|P} * \rho_w(\lambda) \quad (19)$$

7. Correct the measured TOA signal for ozone:

$$\rho_{TOA}^{oz}(\lambda) = \rho_{TOA}(\lambda)/t_{O_3}\lambda \quad (20)$$

8. Eventually compute the Rayleigh calibration coefficient (relative to L1b calibration) by:

$$RA(\lambda) = \frac{\rho_{TOA}^{oz}(\lambda)}{\rho_{TOA}^{theo}(\lambda)} \quad (21)$$

When this procedure is launched pixel-by-pixel, the calibration coefficient of a given observation is computed as the median on all associated pixels (median is found to be more robust than a simple mean).

It is worth underlining the main differences with this method compared to the Hagolle *et al*. (1999) method:

- The marine model is updated from Morel (1988) to Morel and Maritorena (2001);
- The aerosol optical thickness is retrieved at 865 nm by very same approach as operational ocean colour data processing (Antoine and Morel 1999);
- Propagation of the path atmospheric signal from 865 nm to the visible is made directly using the RTM simulations as a function of optical thickness;
- Downward and upward transmittances include the aerosol contribution.

2.2.6 Impact of pressure correction on calibration coefficients

We propose here to analyse the impact of the pressure correction on vicarious calibration coefficients. Because aerosol optical thickness is very low (around 0.02 when $R_{RC}(865)$<0.002), the second order term in the polynomial relationship can be neglected, i.e.

$$\left\{\frac{\rho_{path}}{\rho_R}\right\}(\lambda) \approx XC_0(\lambda) + XC_1(\lambda)\tau_a(\lambda) \tag{22}$$

From previous equations (10)-(14), this allows to write analytically the theoretical path signal by:

$$\rho_{path}(\lambda)_{|P} \approx \rho_R(\lambda)\left(1+\frac{\Delta P}{P_{std}}\eta(\lambda)\right)\left(XC_0(\lambda) + \frac{XC_1(\lambda)}{XC_1(865)}c_\lambda\left(\frac{\rho_{TOA}(865)_{|P}}{\rho_R(865)}\left(1-\frac{\Delta P}{P_{std}}\eta(865)\right) - XC_0(865)\right)\right) \tag{23}$$

In the case there would not be correction for pressure (equivalent to $\Delta P = 0$), we would have:

$$\rho_{path}(\lambda)_{|P_{std}} \approx \rho_R(\lambda)\left(XC_0(\lambda) + \frac{XC_1(\lambda)}{XC_1(865)}c_\lambda\left(\frac{\rho_{TOA}(865)_{|P}}{\rho_R(865)} - XC_0(865)\right)\right) \tag{24}$$

Hence the error in path reflectance would be, at first order in $\Delta P/P_{std}$:

$$\rho_{path}(\lambda)_{|P} - \rho_{path}(\lambda)_{|P_{std}} \approx \left(\eta(\lambda)\rho_{path}(\lambda)_{|P_{std}} - c_\lambda\frac{XC_1(\lambda)}{XC_1(865)}\frac{\rho_R(\lambda)}{\rho_R(865)}\eta(865)\rho_{TOA}(865)_{|P}\right)\frac{\Delta P}{P_{std}}$$

This expression can be further simplified assuming no multiple scattering between aerosol and molecule (again because of very low aerosol content), so that ratio of linear factors $\frac{XC_1(\lambda)}{XC_1(865)}$ is by definition equal to $\frac{\rho_R(865)}{\rho_R(\lambda)}$ (this has been checked with the real LUT coefficients):

$$\rho_{path}(\lambda)_{|P} - \rho_{path}(\lambda)_{|P_{std}} \approx \left(\eta(\lambda)\rho_{path}(\lambda)_{|P_{std}} - c_\lambda \eta(865)\rho_{TOA}(865)_{|P}\right)\frac{\Delta P}{P_{std}} \quad (25)$$

Compared to the single-band expression given in equation (7), this computation shows that impact of pressure partially cancels out due to use of NIR band, when λ get closer to 865 nm. However, the maximum error reached in the blue cannot be neglected since it is approximately:

$$\rho_{path}(412)_{|P} - \rho_{path}(412)_{|P_{std}} \approx 0.14\frac{\Delta P}{P_{std}} \quad (26)$$

The impact of pressure on transmittance is also proportional to $\Delta P/P_{std}$, by a first order development of equation (9):

$$t_{down}(\lambda) * t_{up}(\lambda)_{|P} - t_{down}(\lambda) * t_{up}(\lambda)_{|P_{std}} \approx -\left(t_{down}(\lambda) * t_{up}(\lambda)_{|P_{std}}\frac{1}{2}\tau_R M\right)\frac{\Delta P}{P_{std}} \quad (27)$$

This error is also maximum in the blue, and the order of magnitude is:

$$t_{down}(412) * t_{up}(412)_{|P} - t_{down}(412) * t_{up}(412)_{|P_{std}} \approx -0.30\frac{\Delta P}{P_{std}} \quad (28)$$

Eventually, the relative error that would be produced on $RA(\lambda)$ without correction for pressure is:

$$\frac{RA(\lambda)_{P_{std}} - RA(\lambda)_P}{RA(\lambda)_P} = \frac{\left(\rho_{path}(\lambda)_{|P} - \rho_{path}(\lambda)_{|P_{std}}\right) + \left(t_{down}(\lambda) * t_{up}(\lambda)_{|P} - t_{down}(\lambda) * t_{up}(\lambda)_{|P_{std}}\right)\rho_w(\lambda)}{\rho_{path}(\lambda)_{|P_{std}} + t_{down}(\lambda) * t_{up}(\lambda)_{|P_{std}}\rho_w(\lambda)} \quad (29)$$

For atmospheric and oceanic conditions encountered in the present work, and following previous developments, the maximum error at 412 nm is:

$$\frac{RA(412)_{P_{std}} - RA(412)_P}{RA(412)_P} \approx \frac{(0.14 - 0.30 * 0.04)}{0.19}\frac{\Delta P}{P_{std}} \approx 0.7\frac{\Delta P}{P_{std}} \quad (30)$$

We have assessed the exact relative error of equation (29), by successively activating and de-activating the correction for pressure. Results on MERIS observations (see section 5.1 for

complete details on the parameters) show an excellent agreement with previous order of magnitude at 412 nm, until $\frac{\Delta P}{P_{std}}$=1.5%, i.e. until a pressure of 1028 hPa (Figure 3). At 620 nm the error is of about 0.5$\frac{\Delta P}{P_{std}}$. This proves the need for the pressure correction.

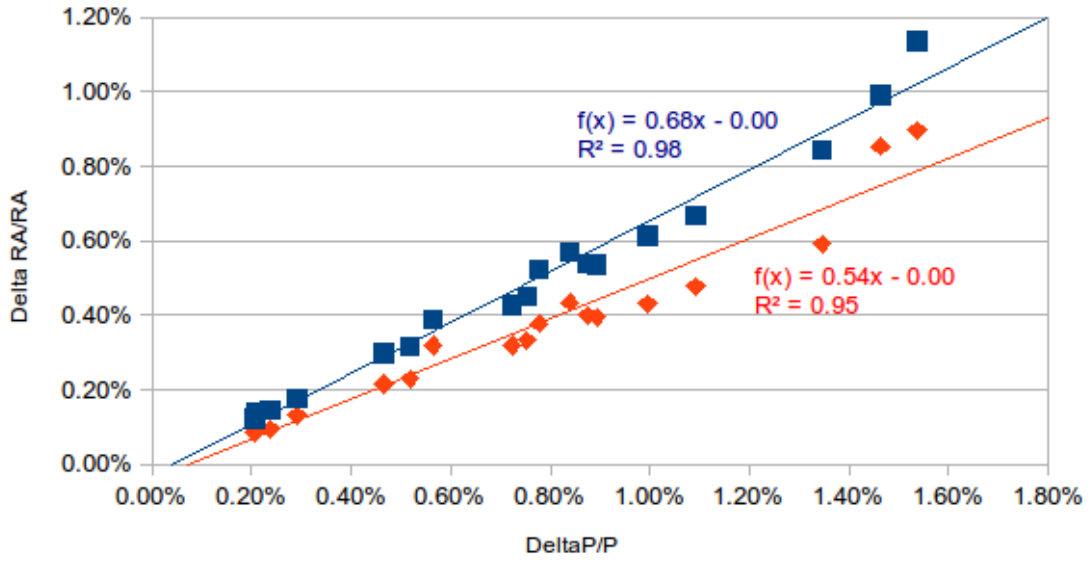

Figure 3 Relative error on the MERIS $RA(\lambda)$ coefficients if there would be no correction for pressure (Y-axis) as a function of the relative pressure change $\frac{\Delta P}{P_{std}}$ (X-axis), at 412 nm(blue) and 620 nm (red). Points are for MERIS acquisition over SPG, see section 5.1.

3 Uncertainty analysis

3.1.1 Published error budget

According to Hagolle *et al* (1999), the following are the main error sources for the methodology:

- Ozone amount (less than 0.5% uncertainty on the calibration at 490 and 443 nm)
- Wind speed: this modifies the sunglint geometry
- Surface pressure: accurately known, it leads to 0.1% on the 3 POLDER channels
- Aerosol amounts: the 865 nm channel is used to discard turbid atmospheres or to estimate aerosol contribution on clear ones. Simulations show that the impact of aerosol model on calibration coefficients is always under 1%. Calibration errors in the 865 nm band also result in some errors in the aerosol correction (5% for 865 nm calibration induces 1% error on 565 and less for 443 and 490 nm).
- The water-leaving radiance is the main uncertainty for the 443 nm channel. An error of 50% on Chlorophyll concentration leads to an uncertainty on calibration coefficient up to 2% for a 443 nm channel.

This leads to a total published uncertainty of 4% maximum. It is worth noting this uncertainty is relatively large considering that calibration coefficients are in practice of around few percent around unity.

3.1.2 Sensitivity analysis on DIMITRI data

The main sources of uncertainty of the vicarious calibration are:

- The input parameters listed above;
- The data screening condition, i.e. mainly clouds;
- The pixel averaged on the calibration region.

Therefore a sensitivity analysis can be conducted with DIMITRI implementation to update the previously mentioned total error budget and to add new terms. We do not recompute uncertainty due to ozone, wind speed and pressure as radiative transfer modellings are analogous between Hagolle *et al* (1999) and DIMITRI. Let us note that the published 0.1% uncertainty due to pressure is in line with our previous analysis, showing that 1.5hPa error lead to 1.5/1013.25*0.7=0.1% error on the calibration coefficient at 412 nm, and less towards the red channels. In the following, the nominal run is a calibration of MERIS over SPG, with default options, in particular a MAR-99 aerosol model.

Sensitivity to clouds coverage: accepting 10% cloud coverage at ROI level, without considering pixel-by-pixel cloud mask, increases the number of calibration points from 19 to 44 and changes the median vicarious coefficients from less than 4% at 412 nm to less than 1% at 665 nm; standard

deviation of individual coefficients is unchanged. This shows that the threshold at 865 nm is not enough to discard cloudy pixels yet well identified by the cloud screening, or possibly their shadows. In conclusion the 0% cloud coverage option at ROI level should be kept for providing less than 5% uncertainty in the blue bands (taking into account other sources of uncertainty), when the pixel-by-pixel cloud mask information is not used.

Sensitivity to aerosol model: switching to model MAR-70 or COAST-70 lead to less than 0.8% error at all bands, slightly higher than in Hagolle *et al*. (1999).

Sensitivity to chlorophyll: replacing the chlorophyll monthly climatology by its extreme values (0.04 and 0.08 mg/m^3 over SPG) impacts on average the coefficients from 3% at 412 nm to 0.15% at 665 nm. We thus retrieve the conclusion of Hagolle *et al*. (1999), that the main driver of Rayleigh vicarious calibration is the chlorophyll concentration, in particular in the blue wavelengths.

Sensitivity to sensor noise (pixel averaging): this can be assessed by comparing the DIMITRI output coefficient starting either from the averaged TOA signal, or from the pixel-by-pixel extraction (see section 3.3.3 about this processing mode). A first effect of using the averaged mode is to decrease even more the number of calibration points (from 19 to 9), while not improving the calibration coefficient dispersion. The impact is of about 1.3% at 412 nm and less than 1% at other bands.

The total error budget is about 5.9% at 412 nm and slightly lower than 4% at other bands (Table 2). This high uncertainty at 412 nm is an extreme case, due to sensitivity of marine reflectance (see e.g. Figure 8 in Morel and Maritorena, 2001). If we consider that errors on the input parameters are random (around true pressure, ozone, chlorophyll, etc.), this error budget contains mainly (at first order) the random uncertainty, on punctual calibration points. However systematic input errors would produce systematic error on calibration coefficients. Hence the exact structure of input error should be assessed in future studies.

Table 2: Uncertainty budget of DIMITRI Rayleigh vicarious calibration coefficients, from sensitivity analysis, decomposed by sources. (*) comes from Hagolle *et al*. (1999)

Band	Ozone (*)	Wind (*)	Pressure (*)	Aerosol	Chlorophyll	Pixel	Total
412		0.5%	0.1%	1%	3.0%	1.3%	5.9%
443		0.5%	0.1%	1%	2.5%	0.7%	4.8%
490		1%	0.1%	1%	0.5%	0.1%	2.7%
510		1%	0.1%	1%	0.2%	0.7%	3.0%
560	0.5%	1.5%	0.1%	1%	0.5%	1.0%	4.6%
620		1.5%	0.1%	1%	0.2%	0.9%	3.7%
665		1.5%	0.1%	1%	0.1%	0.3%	3.0%

3.1.3 Tentative random/systematic uncertainty breakdown

Since vicarious calibration aims eventually at providing a unique set of coefficients, by averaging all targets, the uncertainty budget should rigorously be split into:

- The random uncertainty: its contribution to the averaged calibration coefficient goes down as more calibration points are considered
- The systematic uncertainty: its contribution remains the same whatever the number of points

No systematic source of error has been theoretically identified in previous uncertainty budget. Hence, we have tried to assess it experimentally, with real MERIS vicarious coefficients at SPG (most rigorous case study at present time due to knowledge of auxiliary data and proper radiative transfer LUT), as described in section 5.1. Let us note σ the standard-deviation of a single target coefficient, i.e. the random uncertainty, and $\sigma(\overline{RA})$ the standard-deviation after averaging N targets; one has

$$\sigma(\overline{RA}) = \frac{\sigma}{\sqrt{N}} \tag{31}$$

Despite only few points are available (18, see section 5.1), we observe that the experimental dispersion on $\overline{RA}$ does not follow this shape when N varies from 2 to 18. Assuming that the observed dispersion can be understood as the mean square error (MSE), we have searched the bias and random uncertainty following this decomposition:

$$MSE(N) = Bias^2 + \left(\frac{\sigma}{\sqrt{N}}\right)^2 \tag{32}$$

In practice this is realised through a linear fit on $MSE(N) * N$. In order to avoid any statistical artefact when increasing the sample from N=2 to 18, we order it randomly and average over a large number of realisations (10 000).

Results of bias and σ are provided on Figure 4, and compared with previous sensitivity uncertainty budget. They present a smooth variation with wavelength and are roughly of same order of magnitude, from 8% at 412 nm to 1% at 665 nm. Extrapolating these numbers on a large number of targets, i.e. decreasing at maximum the random contribution, results into a bias of less than 6%.

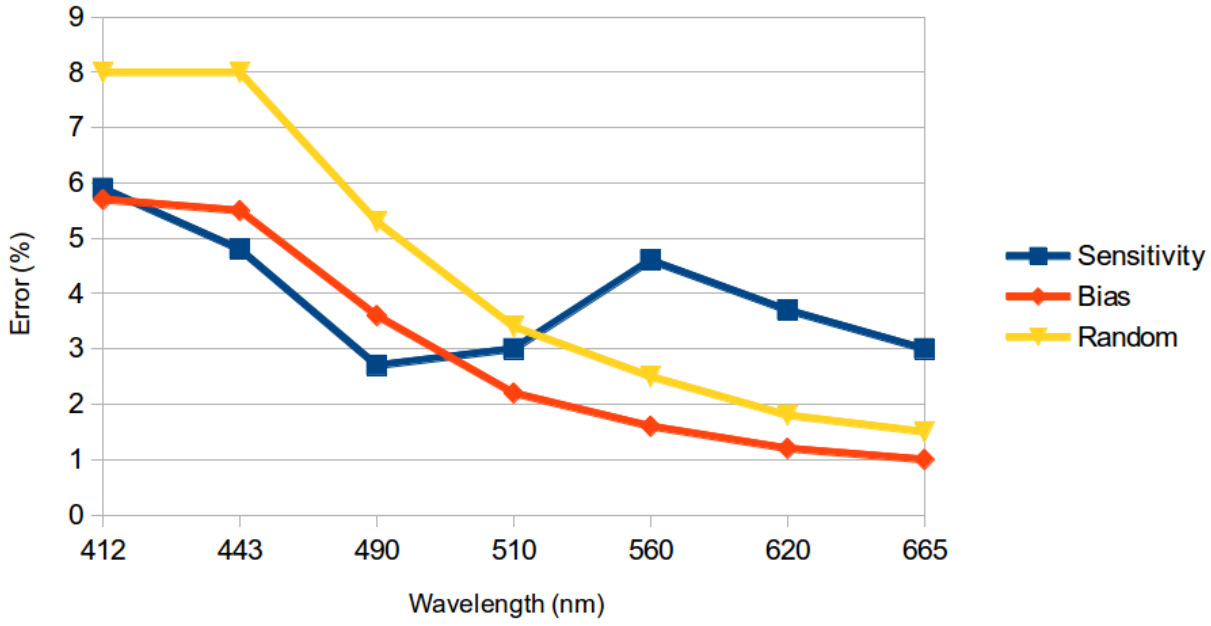

Figure 4 Tentative random (yellow)/bias(red) uncertainty breakdown of Rayleigh vicarious method, based on MERIS vicarious coefficients at SPG. Blue uncertainty is from the sensitivity study of section 3.1.2

The uncertainty budget derived here gives the overall accuracy of the method and should be improved. A way to derive a rigorous uncertainty budget would be to specify the random and systematic errors of each input parameter (e.g. chlorophyll, pressure, etc.) and to propagate both components into the methodology up to the simulated TOA reflectances. Such work is recommended for future DIMITRI releases.

4 Implementation in DIMITRI_v3.0

4.1 Radiative transfer Look up tables (LUT)

4.1.1 Format specification in DIMITRI

For every sensor (i.e. every set of wavelengths and spectral responses), DIMITRI Rayleigh calibration needs one Rayleigh LUT and four other LUT for each considered aerosol models: aerosol optical thickness dependence, downward total transmittance, upward total transmittance and path over Rayleigh fitting coefficients as function of optical thickness (previously noted XC in section 2.2.4).

All LUTs must be written in text file, with space as the field separator, following the naming convention of Table 3 to Table 7 below (AER may be any ASCII field identifying the aerosol model) and placed in directory AUX_DATA/RTM/SENSOR/. Any LUT satisfying this convention is detected by the GUI and can be used for the Rayleigh calibration. Reading and interpolation routines of DIMITRI_v3.0 are based on header description, giving size and discretisation of the LUT; this allows totally generic sampling in the LUT. Only the wavelengths must exactly follow those of the considered sensor, as defined in the Bin/DIMITRI_Band_Names.txt configuration file (NaN or any field may be used if some bands are not processed in the RTM).

Table 3: RHOR_SENSOR.txt template for Rayleigh reflectance LUT (PARASOL example)

PARASOL rayleigh reflectance
lambda: 443 490 565 670 763 765 865 910 1020
thetas: 0.0 10.222899999999999 21.347999999999999 32.478999999999999 43.611400000000003 54.744399999999999 65.877600000000001 77.010999999999996 85.0
thetav: 0.0 10.222899999999999 21.347999999999999 32.478999999999999 43.611400000000003 54.744399999999999 65.877600000000001 77.010999999999996 85.0
deltaphi: 0.0 45.0 90.0 135.0 180.0
wind: 1.5 5.0 10.0
Inner loop is on wind, then deltaphi, thetav, thetas and bands
Dimensions: 9 9 9 5 3
0.093101002156892598
…

Table 4: TAUA_SENSOR_AER.txt template for spectral dependence of aerosol optical thickness LUT at given AER model (PARASOL example for MAR-99)

PARASOL aerosol optical thickness for aerosol MAR99V # Columns gives tau_a corresponding to 7 reference optical thickness at 550 nm, see DIMITRI ATBD Methodology for Vicarious Calibration # (first optical thickness is zero) # lambda: 443 490 565 670 763 765 865 910 1020 # Dimensions: 9 7 0.0 0.048365032840822532 0.06891816636709823 0.14085534900228486 0.34638948316831686 0.55199815122619944 0.8600978983396802 …

Table 5: TRA_DOWN_SENSOR_AER.txt template for downward total transmittance LUT at given AER model (PARASOL example for MAR-99)

PARASOL total downward transmittance (direct+diffuse, Rayleigh+aerosol) for aerosol model MAR99V # Columns gives t_up for 7 aerosol optical thickness (total, i.e. all layers) given in file TAUA_PARASOL.txt # (first optical thickness is zero hence gives Rayleigh transmittance) # lambda: 443 490 565 670 763 765 865 910 1020 # thetas: 0.0 10.222899999999999 21.347999999999999 32.478999999999999 43.611400000000003 54.744399999999999 65.877600000000001 77.010999999999996 85.0 # Inner loop is on thetas, then on bands # Dimensions: 9 9 7 0.90230878440213247 0.89548770811881195 0.89443874044173644 0.89082490644325962 0.88180250936785953 0.87149871603960372 0.85586978330540764…

Table 6: TRA_UP_SENSOR_AER.txt template for upward total transmittance LUT at given AER model (PARASOL example for MAR-99)

PARASOL total upward transmittance (direct+diffuse, Rayleigh+aerosol) for aerosol model MAR99V # Columns gives t_up for 7 aerosol optical thickness (total, i.e. all layers) given in file TAUA_PARASOL.txt # (first optical thickness is zero hence gives Rayleigh transmittance) # lambda: 443 490 565 670 763 765 865 910 1020 # thetav: 0.0 10.222899999999999 21.347999999999999 32.478999999999999 43.611400000000003 54.744399999999999 65.877600000000001 77.010999999999996 85.0

```
# Inner loop is on thetav, then on bands
# Dimensions: 9 9 7
0.90239652667174386 0.8954501151256663 0.89439713998476766 0.89094964438690016
0.88187861303884252 0.8717368052399086 0.85580240600152335 …
```

Table 7: XC_SENSOR_AER.txt template for XC fitting coefficients LUT at given AER model (PARASOL example for MAR-99). Coefficients in column are respectively for the 0, 1 and 2-order term of the polynomial

```
# PARASOL XC coefficients of rhopath/rhoR fit against optical thickness for aerosol model MAR99V
# Columns gives the 3 XC coefficients
# Inner loop is on wind, then deltaphi, thetav, thetas and bands
# lambda: 443 490 565 670 763 765 865 910 1020
# thetas: 0.0 10.222899999999999 21.347999999999999 32.478999999999999
43.611400000000003 54.744399999999999 65.877600000000001 77.010999999999996 85.0
# thetav: 0.0 10.222899999999999 21.347999999999999 32.478999999999999
43.611400000000003 54.744399999999999 65.877600000000001 77.010999999999996 85.0
# deltaphi: 0.0 45.0 90.0 135.0 180.0
# wind: 1.5 5.0 10.0
# Dimensions: 9 9 9 5 3 3
1.0  2.002697662147753 -0.81783546808834739…
```

4.1.2 Atmospheric radiative transfer LUTs generation

This section describes the generation of the look-up tables of atmospheric path reflectance, total transmission and relative optical thickness over wavelength as required by both the Rayleigh calibration and the sunglint calibration in DIMITRI. The look-up tables required are almost identical in structure to those used in the MERIS atmospheric correction scheme (Antoine and Morel 2011, Barker *et al*. 2012), but must be generated for every band of every sensor contained in DIMITRI. Currently these bands cover wavelengths from 340 nm to 5000 nm. While the Rayleigh correction requires wavelengths up to 700 nm, plus some in the NIR for aerosol detection, the glint calibration requires these tables at all wavelengths. Since many of the sensors in DIMITRI cover the same wavelength ranges the approach that has been taken is to produce one overall hyperspectral look-up table that can be convolved to each sensor band using the relative spectral response function (RSR) of each band. This approach makes the modelling more efficient and has the benefit that if new sensors are added to DIMITRI their Rayleigh and glint calibration look-up tables can be generated without further modelling, as long as the wavelengths are in the range 340 to 5000 nm.

4.1.3 Computational considerations

As the values required are for a Rayleigh scattering based calibration it is required to calculate them to the highest accuracy possible, which means they must be fully vectorial (with polarisation) since scalar modelling can introduce deviations of a few percentage in Rayleigh scattering (Hedley et al . 2013). Here, we have used a modified version of the libRadtran Monte Carlo model Mystic (Mayer and Kylling 2005; Mayer 2009). This model is capable of vectorial or scalar modelling and the vectorial mode Rayleigh scattering has been validated against both the MERIS atmospheric correction look-up tables and an independent model, Siro, developed at the Finnish Meterological Institute (Kujanpää 2013) (Figure 3).

The disadvantage of Mystic is that it is computationally slow, and being a Monte Carlo model is subject to statistical noise if insufficient computational effort is applied. In particular, with Mystic, each individual solar-view geometry requires a fully independent model run. Other models, such as the scalar Disort, can typically output results for a set of view zenith angles and relative azimuths for each run, but with Mystic one run must be done for every combination of solar, view and relative azimuth angles. These computational considerations are not trivial and require some compromises to be made. On a standard workstation, to produce results with the statistical convergence shown in Figure 3 takes approximately 15 seconds per Mystic run on average (the run time increases with aerosol optical thickness). The MERIS atmospheric correction look-up tables are tabulated over 25 zenith angles, 23 azimuth angles, 3 wind speeds, 7 aerosol optical thicknesses. If tables were to be generated at this resolution at 400 wavelengths, for example, then the computation time would be 25 x 25 x 23 x 3 x 7 x 400 x 15 seconds = 57 years. Therefore a compromise has been made in terms of the angular resolution of the modelling (Table 8). Modelling at every nanometre is unfeasible so 386 wavelengths from 340 – 5000 nm have been chosen as outlined in Table 8. This wavelength choice means that even the narrowest bands, MERIS at 9 nm, will have a minimum of two tabulated values within their RSR, but most will have many more. Conversely for bands that are wide this method ensures they are based on results spread across the band width. For the structure in Table 8, running the look-up table generation on a high-end workstation where calculation can be parallelised in up to 12 concurrent processes enables a look-up table for one aerosol model to be generated in approximately 4 weeks of compute time.

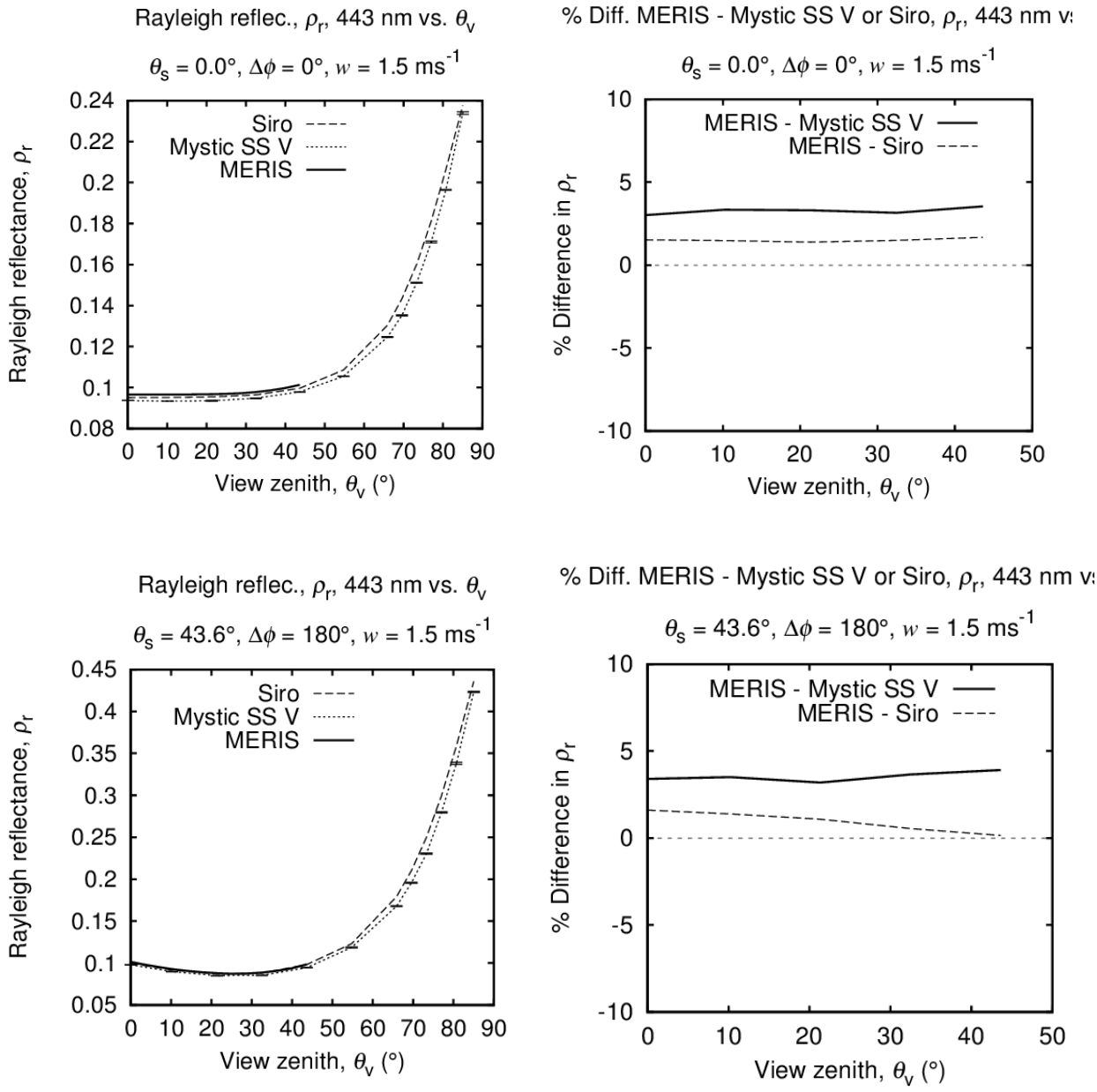

Figure 5: Example Rayleigh scattering results from Hedley *et al*. (2013) at 443 nm, from the MERIS atmospheric correction look-up tables and from Mystic and Siro in spherical shell vectorial mode.

Left side: Rayleigh scattering with error bars showing ±1 standard error on the mean for Mystic results. *Right side*: corresponding percentage difference between MERIS and Siro, and MERIS and Mystic.

Note: both Mystic and Siro predict an error of only one third of a percent due to plane parallel versus spherical shell modelling at zero solar and zenith angles, hence this is not an explanation for the small deviations of 2 – 3% seen here.

4.1.4 Details of the required tables

The required tables are as follows:

1. Atmospheric path reflectance

This is calculated over a 'black ocean', i.e. the bottom boundary is a wind-blown air water interface but below surface reflection is zero. The direct reflectance path from the surface is excluded so that the reflectance represents photons that have undergone one or more atmospheric scattering events. To evaluate this requires a modification to the Mystic code to exclude photons that have not undergone an atmospheric scattering event. Note, gaseous absorption is also excluded in this calculation as this is corrected for elsewhere. What is actually stored in the look-up tables is the path reflectance, ρ_{path}, divided by the Rayleigh reflectance, ρ_r, as a function of aerosol optical thickness, fit to a quadratic function for each view and solar geometry, wind speed and sensor band. The quadratic fit is constrained so that the constant term is 1 as for $\tau_a(b) = 0$, $\rho_{path}(b) / \rho_r(b) = 1$ (where b is the sensor band). See Hedley *et al* (2013) for more information on the accuracy of this function fitting.

2. Total transmission, upward and downward

The product of the total transmission upward and downward is evaluated from Mystic using another modification that excludes photons that have not reflected from the bottom boundary. The model is run over a Lambertian bottom of diffuse reflectance 0.1, the total transmittance is then the reflectance divided by 0.1 and corresponds to the assumption that water-leaving reflectance has a Lambertian BRDF. This assumption, while not strictly accurate (Morel and Gentili, 1993), will have minimal impact in this context. The assumption of Lambertian sub-surface reflectance has been shown to introduce only small errors (Yang and Gordon, 1997), see further discussion on this issue in Hedley *et al.* (2013). In addition the Lambertian assumption allows decoupling of the upward and downward transmittances, since the bottom boundary reflectance only has a dependence on the cosine of the solar zenith angle. The algorithm input requires that the upward and downward total transmittances be tabulated separately, although it is only their product that is used (Eqn. 12). If the model is run with a full set of solar zenith angles with view angle fixed (e.g. at zero) and vice versa the individual upward and downward transmissions could be calculated except there is unavoidably an unknown scaling factor between the upward and downward transmissions. In other words, for n zenith angles, there are $2n$ unknowns, but only $2n$-1 values to derive these from. This can be solved by assuming the upward and downward transmissions at zenith angle zero are equal. Note this is simply a trick to enable the algorithm implementation to be supplied with separate tables for upward and downward transmittance. When the product is formed the unknown factor disappears and the correct total transmission is used in Eqn. 12 regardless of this assumption.

This reflectance-based method for deriving the transmittance is required and appropriate because: 1) Mystic in general lacks outputs from which the total transmittances can be easily

computed, and 2) it is the inverse of the process that must be captured, i.e. the reconstruction of the TOA reflectance from the bottom boundary reflectance (Eqn. 12). Decoupling of the water leaving reflectance from the atmospheric radiative transfer is equivalent to assuming that higher order photon interactions at the bottom boundary are negligible, i.e. that a photon reflects once only from the water body and hence the TOA reflectance is a linear function of the water body reflectance. This is valid, at least for diffuse reflectances up to 0.1, as shown in Figure 6 (see also Hedley *et al* 2013).

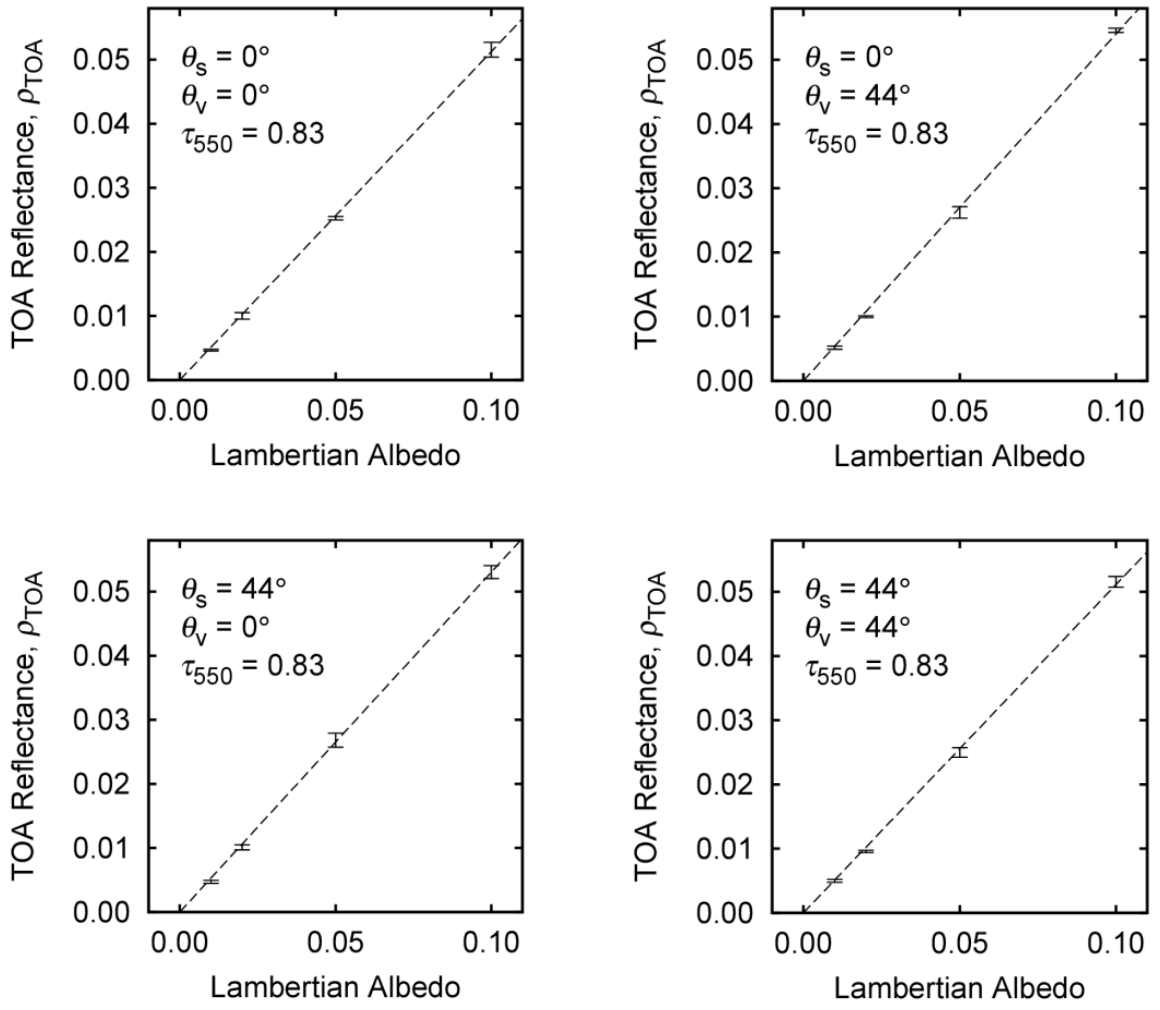

Figure 6: TOA reflectance from diffuse transmission paths as a function of bottom boundary Lambertian albedo from Hedley *et al*. (2013). These results were calculated in scalar spherical shell Mystic with the MAR-99 aerosol model (MERIS aerosol no. 4) τa (550) = 0.83, but the general conclusion of linearity with bottom reflectance will hold for plane parallel vectorial modelling. Error bars are ± 1 standard error on the mean, line is least squares linear fit.

3. Variation in optical thickness with band

The radiative transfer models are run with aerosol models of differing specified optical thicknesses at wavelength 550 nm. The algorithms require that the corresponding aerosol optical thickness can be derived for other bands. This table enables that transformation to be made, for a given sensor and aerosol model it relates the optical thickness in one band to the others. These values are not dependent on solar-view geometry or wind speed. The values at each wavelength are output directly in the libRadtran run log at each wavelength. The values for each sensor band are derived from the convolution by the sensor RSR.

4.1.5 Details of libRadtran parameterisation

Certain details of the libRadtran parameterisation are listed below for reference. The next section describes the aerosol models.

- Standard US atmosphere 'AFGLUS'
- Atmospheric height 120 km
- Pressure 1013 mb
- No gaseous absorption
- Plane parallel configuration
- Vectorial scattering
- For black ocean, non-vectorial Cox-Munk wind-blown sea surface

Mystic can also be run in spherical shell mode, and even for solar and zenith angles of zero this can make a third of a percentage difference in the Rayleigh scattering, and for other solar-view geometries the deviation can rise to several percent (Hedley *et al*. 2013). While the LUT generation code permits switching to spherical shell mode, within the context of this project the 'traditional' plane parallel assumption has been made.

Similarly, while Mystic does incorporate a vectorial version of the sea surface BRDF function, the vast majority of previous work, such as the MERIS atmospheric correction LUTs, has utilised the non-vectorial mode Cox and Munk equations, and these are used here. Use of a vectorial sea surface function, or one that is more accurate in that it incorporates elevation statistics as well as slope (Kay *et al*. 2012) may be advisable, but is a potential future research topic.

Testing indicated that the Mystic options for forward or backward ray tracing and the 'vroom' optimisation did not reduce processing time or produce any overall improvement in statistical convergence. The 'escape' photon optimisation was enabled throughout.

Table 8: Structure of look-up tables for one aerosol model.

Parameter	Units	n	Values
λ	nm	386	340 to 1100 with step 4 (191), 1120 to 5000 step 20 (195)
θ_s	deg.	9	0, 10.2229, 21.3480, 32.4790, 43.6114, 54.7444, 65.8776, 77.0110, 85.0
θ_v	deg.	9	0, 10.2229, 21.3480, 32.4790, 43.6114, 54.7444, 65.8776, 77.0110, 85.0
$\Delta\phi$	deg.	5	0, 45, 90, 135, 180
wind	ms^{-1}	3	1.5, 5, 10
$\tau_a(550)$	-	7	0, 0.04, 0.06, 0.13, 0.33, 0.53, 0.83

Table 9: Components used in OPAC aerosol models as implemented in libRadtran (Hess et al. 1998)

Code	Meaning
inso	insoluble
waso	water_soluble
soot	soot
ssam	sea_salt_accumulation_mode
sscm	sea_salt_coarse_mode
minm	mineral_nucleation_mode
miam	mineral_accumulation_mode
micm	mineral_coarse_mode
mitr	mineral_transported
suso	sulfate_droplets

4.1.6 Aerosol models

Since generating a table for one aerosol model takes approximately 4 weeks of computation time, it is not trivial to add many aerosol models to the algorithm. Within the scope of the prototype algorithm three models have been incorporated.

- **MC50:** the OPAC Maritime clean model included in libRadtran
- **MAR50:** the MERIS atmospheric correction aerosol model no. 1
- **MAR99:** the MERIS atmospheric correction aerosol model no. 4

Details of the aerosol model parameterisations are given in the following two sections. Figure 7 shows aerosol optical thicknesses as a function of wavelength for the three models, as output by libRadtran, and indicates that MAR50 and MAR99 are correctly set-up as corresponding to the MERIS atmospheric correction LUT models. Interestingly although the OPAC model MC50 is

described as corresponding to 50% relative humidity in the libRadtran documentation, it corresponds closely to MAR99, which is considered as 99% relative humidity. However the slope of MC50 starts to deviate in the Near-Infra Red, so it is worthwhile to retain it in the algorithm. MAR50 and MAR99 represent the extreme slopes in optical thickness from the MERIS maritime aerosol models, so candidate models for future inclusion might be MAR70 and MAR90 which represent intermediate slopes.

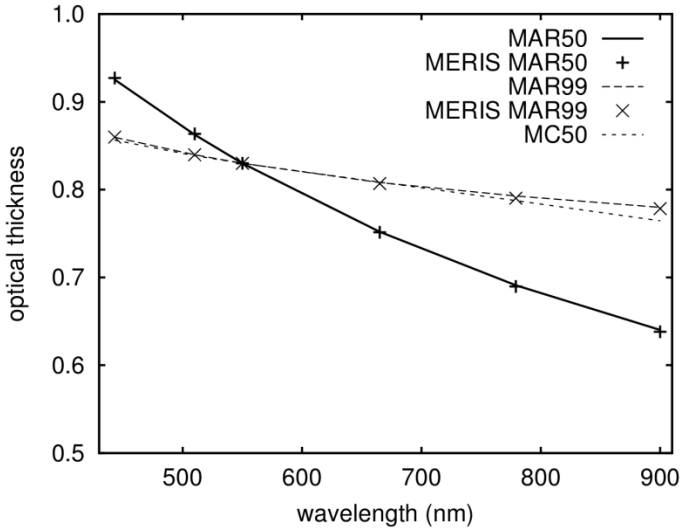

Figure 7: Aerosol optical thickness from 440 to 900 nm for the implemented aerosol models MAR50, MAR99 and MC50. Tabulated values for MAR50 and MAR99 from the MERIS atmospheric correction algorithm are also shown as point data.

MC50 - OPAC Maritime Clean Aerosol Model

The libRadtran OPAC "Maritime clean" model (Hess *et al*. 1998) corresponds to relative humidity of 50% and as implemented in libRadtran corresponds to a fixed vertical profile of six aerosol types specified up to 35 km, which combined have aerosol optical thickness of 0.136 at 550 nm. In order to generate a look up table parameterised over aerosol optical thickness, $\tau_a(550)$, it is necessary to scale the mass densities or some or all of the components. In the MERIS atmospheric correction aerosol models the way this is achieved is by holding constant the profiles above 2 km and scaling only the 0 – 2 km components, so this practice has been followed in the scaling of the OPAC MC50 model. MC50 in libRadtran contains the following components (Table 9): inso, waso, soot, ssam, sscm, suso. Of these, inso, soot, and suso only occur above 2 km, ssam and sscm occur only below 2 km and waso occurs up to 12 km but is 5-10 times denser below 2 km. Therefore splitting the model into variable 0 – 2 km profiles and fixed profiles above 2 km is supported by the construction of the model and involves only varying the water soluble and sea salt aerosols. In MC50 the fixed profiles above 2 km correspond to an aerosol optical thickness of 0.018, in

comparison to 0.030 in the MERIS standard aerosol models 1-12. The default MC50 0 – 2 km profiles have an optical thickness of 0.119, and the mass densities in this fraction are scaled linearly to give the total $\tau_a(550)$ as required in the look up table construction (Table 8). The default MC50 corresponds approximately to the tabulated point $\tau_a(550) = 0.13$. The libRadtran OPAC models are defined from 250 nm to 40 microns, hence in terms of wavelength coverage are more than adequate.

MAR50 and MAR99, the MERIS atmospheric correction models

These models have been constructed for use in vectorial mode Mystic by use of the mie scattering tool supplied with libRadtran. The size distributions and refractive indices of the model components used are specified in the MERIS RMD and original paper by Shettle and Fenn (1979). The mie tool is used to generate the wavelength dependent Mueller matrices and single scattering albedos, and these are conveniently output in netCDF files that libRadtran takes as input. An additional input file specifies the vertical profiles of the differing aerosol components, which for these models occur in three distinct layers, 0 -2 km, 2 -12 km and 12 – 50 km. Again, the relative proportions were fixed according to the values in the MERIS RMD (Barker *et al*. 2012), but the 0 - 2 km fraction was scaled to reach the required $\tau_a(550)$ values as in Table 8.. The models were validated by checking the relative optical thicknesses at different wavelengths to those tabulated in the MERIS RMD. Barring numerical differences in the modelling and undocumented details in the parameterisation, the MAR50 and MAR99 models should correspond exactly to hyperspectral versions of models 1 and 4 in the MERIS atmospheric correction.

4.2 Auxiliary data for marine modelling

Pure seawater absorption and scattering coefficients come from the NASA ocean color repository: http://oceancolor.gsfc.nasa.gov/DOCS/RSR/water_coef.txt.

The table of averaged cosine for downwelling reflectance (μ_d in Morel (1988) and Morel and Maritorena (2001)) comes from Morel *et al*. (2006) available on LOV repository at oceane.obs-vlfr.fr/pub/morel. Other parameters of the Morel and Maritorena (2001) model are directly taken from their table 2.

As suggested by the sensitivity analysis, deriving meaningful coefficients needs the most realistic chlorophyll estimate. Unfortunately we cannot fully benefit from the unique characterisation of oceanic calibration zones by Fougnie *et al*. (2002) because DIMITRI SPG and SIO sites do not exactly coincide with these regions. For SPG, we can still consider as a last resort the characterisation of the South-East Pacific zone (PacSE); more precisely we use updated statistics of ACRI-ST reported in Figure 8:, showing chlorophyll concentration variation between 0.045 and 0.075 mg/m3 along the year. In order not to slant the MERIS and MODIS calibration results, we only consider SeaWiFS time-series, monthly averaged in DIMITRI.

Such time-series cannot be created similarly for DIMITRI SIO site, located in a much more variable

and richer region than IndS zone (Indian South) of Fougnie *et al*. (2002); in this case users can select a fixed value of their choice in DIMITRI HMI (see hereafter).

Note that users can still add any chlorophyll climatology file, which would be automatically processed by DIMITRI.

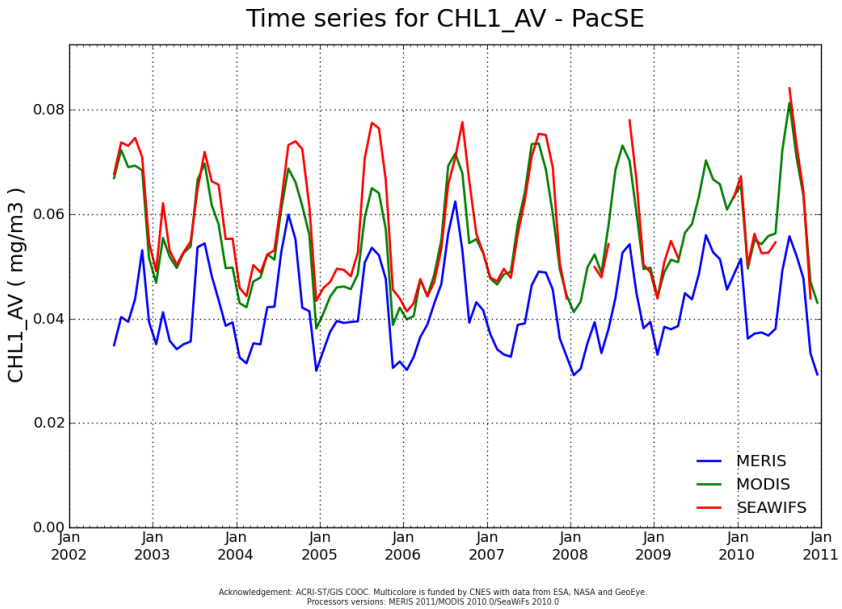

Figure 8: Time series of chlorophyll concentration over South-East Pacific calibration zones for MERIS, MODIS and SeaWiFS. Products and statistics processed by ACRI-ST and distributed on the GIS COOC data portal in the frame of the MULTICOLORE project, funded by CNES (MSAC/115277), using ESA ENVISAT MERIS data and NASA MODIS and SeaWiFS data.

4.3 Pixel-by-pixel versus averaged extraction

Whereas the DIMITRI v2.0 database only stores spatially averaged L1b information per acquisition (array SENSOR_L1B_REF in SENSOR_TOA_REF.dat files for each site and sensor), DIMITRI v3.0 also retains the pixel-by-pixel extractions in new SENSOR_TOA_REF_PIX.dat files. In IDL, the parameters and dimensions of new arrays SENSOR_L1B_REF_PIX are based on former averaged SENSOR_L1B_REF arrays but:

- They include cloud mask as a new parameter. The list of parameters is thus: decimal_time, VZA, VAA, SZA, SAA, Cloud_mask, Ozone, Pressure, Humidity, Zonal_wind, Meridional_wind, Water_vapour, rho_band_0, …, rho_band_n
- They store each parameters for all individual pixels falling within the site, instead of the mean and standard-deviation; storage follows the same logics as averaged arrays when more than one viewing directions is available (e.g. AATSR, ATSR2, PARASOL):

  obs1_dir1_pix1, ..., obs1_dir1_pixO_1D_1, obs1_dir2_pix1, ..., obs1_dir2_pixO_1D_2, ...

where O_iD_j is the number of pixels for observation, i, in direction j.

It is worth noting that this number is in all generality variable through all observations and directions, because of variable sensor coverage of the site and variable pixel size in the swath. Also, there is no data screening of the pixels during the DIMITRI ingestion, contrary to the average restricted to valid pixels (validity based on radiance thresholds only, not cloudiness).

As a consequence the size of new SENSOR_TOA_REF_PIX.dat files (one per site and sensor/processing version) is substantially bigger than that of SENSOR_TOA_REF.dat but still largely lower than the archive of raw L1b product. As an example, the total size of the current MODISA archive over SPG site is:

- 2.7MB in averaged extraction file,
- 1.5GB in pixel-by-pixel extraction file, and
- 167 GB in raw L1B files.

The pixel-by-pixel extractions allow vicarious calibration coefficients to be computed on exact pixel radiometry, then averaged per scene. Furthermore it allows to increase the number of calibration observations (still selecting the 0% cloud coverage as we highlighted in the sensitivity analysis), since some clear pixels may pass some tests (Rayleigh correction test at 865 nm) whereas the averaged signal does not. Even though selecting perfectly homogeneous scenes is a preferred condition for calibration, the pixel mode is a practical way to maximise with good confidence the number of usable data in the current DIMITRI database, limited to only two oceanic sites; as a reminder Hagolle *et al*. (1999) used nine oligotrophic oceanic regions.

The user is given the choice to select either this pixel-by-pixel extraction or the standard DIMITRI averaged extraction (see HMI updates hereafter).

4.4 Output files generated by the Rayleigh calibration

Six types of files are systematically generated for each Rayleigh vicarious calibration run:

1. **RAYLEIGH_CAL_LOG.txt:** log file summarising all options of the run (parameters).
2. **RAYLEIGH_CAL_SITE_SENSOR_PROC_AVG.dat:** IDL SAV file storing array VIC_COEF_AVG of averaged vicarious coefficients per observation (when pixel by pixel mode) or directly coefficients starting from the averaged TOA signal (if not) and associated uncertainties. Consistently with the standard SENSOR_TOA_REF.dat DIMITRI files, parameters of VIC_COEF_AVG array are:

   decimal_time, VZA, VAA, SZA, SAA, Ozone (avg+stddev), Pressure (avg+stddev), Humidity (avg+stddev), Zonal_wind (avg+stddev), Meridional_wind (avg+stddev), Water_vapour (avg+stddev), DAk_band_0, …, DAk_band_n, DAk_unc_band_0,…DAk_unc_band_n

3. **RAYLEIGH_CAL_SITE_SENSOR_PROC_AVG.csv:** same as previous but in csv format for direct reading.
4. **RAYLEIGH_CAL_SITE_SENSOR_PROC_STAT.csv:** csv file containing statistics on the final unique set of coefficients per wavelength (median, mean, standard-deviation, number of points, mean uncertainty).
5. **RAYLEIGH_CAL_SITE_SENSOR_PROC_MEAN.JPG:** plot of the mean coefficients as a function of wavelength.
6. **RAYLEIGH_CAL_SITE_SENSOR_PROC_WAV.JPG:** plots for each wavelength, of the time-series of averaged coefficients.

When the pixel-per-pixel mode is activated, another output is:

7. **RAYLEIGH_CAL_SITE_SENSOR_PROC_PIX.dat:** IDL SAV file identical to the _AVG.dat one's but providing information for all individual pixels, consistently with input SENSOR_TOA_REF_PIX.dat file. It stores array VIC_COEF, whose parameters are:
   decimal_time, VZA, VAA, SZA, SAA, Cloud_mask, Ozone, Pressure, Humidity, Zonal_wind, Meridional_wind, Water_vapour, DAk_band_0, …, DAk_band_n, DAk_unc_band_0,…DAk_unc_band_n
   Averaged calibration coefficients per observation are exactly identical to the coefficients of VIC_COEF_AVG array provided in _AVG.dat file.

4.5 DIMITRI modules/functions/architecture

The Rayleigh calibration methodology is implemented as an individual IDL module, called by a new GUI module (or directly in command line); it then calls several separated routines for specific jobs (e.g. computation of Rayleigh reflectance, of marine models, etc.). All routines related to the Rayleigh vicarious calibration are stored in the Source/vicarious directory. Except for the GUI, there is no interaction with previous DIMITRI_v2.0 modules.

Schematically, the main Rayleigh calibration module:

- Interfaces with the DIMITRI database to identify appropriate L1b extractions with respect to chosen region, sensor, processing version and year;
- Screens data for ROI cloud and region coverage; in the pixel-by-pixel mode, pixels are further screened by the cloud mask;
- Finds all pixels within other user defined parameters specific to the calibration method;
- Reads all RTM LUT;
- Performs the Rayleigh Calibration band per band;
- Post-processed the coefficients (averaged, statistics);
- Outputs the individual and averaged calibration coefficients for each band in several text and image file, as defined in section 4.4.

4.6 HMI updates and User options

The Rayleigh calibration methodology allows both GUI and command line activation. The main DIMITRI_v3.0 window is updated from DIMITRI_v2.0 for using the GUI mode (Figure 9:).

All processing parameters specific to the Rayleigh calibration are selectable by the user through a new window (Figure 9):

- Case study (region, sensor, processing version, year, output directory);
- Cloud and region coverage percentage; note that scenes having a manual cloud screening set to 0 will be selected whatever the automated cloud screening value;
- Pixel-by-pixel mode;
- Chlorophyll concentration, either by monthly climatology put in the DIMITRI auxiliary folder or by a fixed values;
- Maximum wind speed;
- Maximum Rayleigh corrected normalised radiance at 865 nm;
- Aerosol model, among an automated list built on all models existing in DIMITRI auxiliary folder, sensor per sensor.

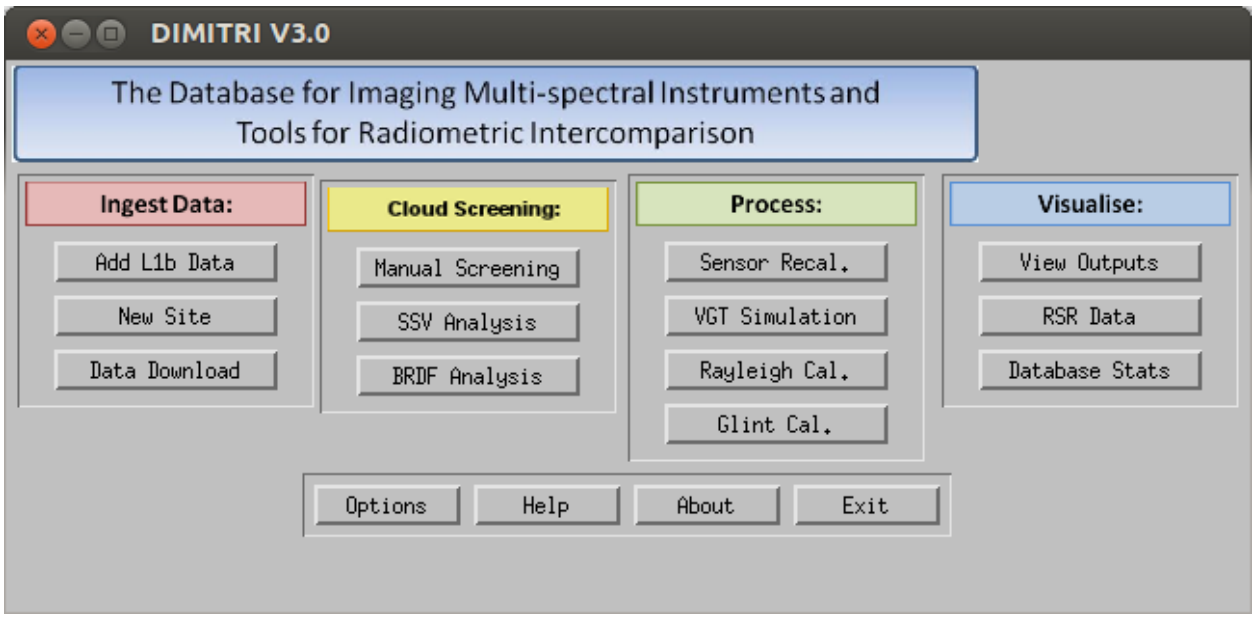

Figure 9: Main DIMITRI window updated for Rayleigh scattering and Sunglint vicarious calibration methods

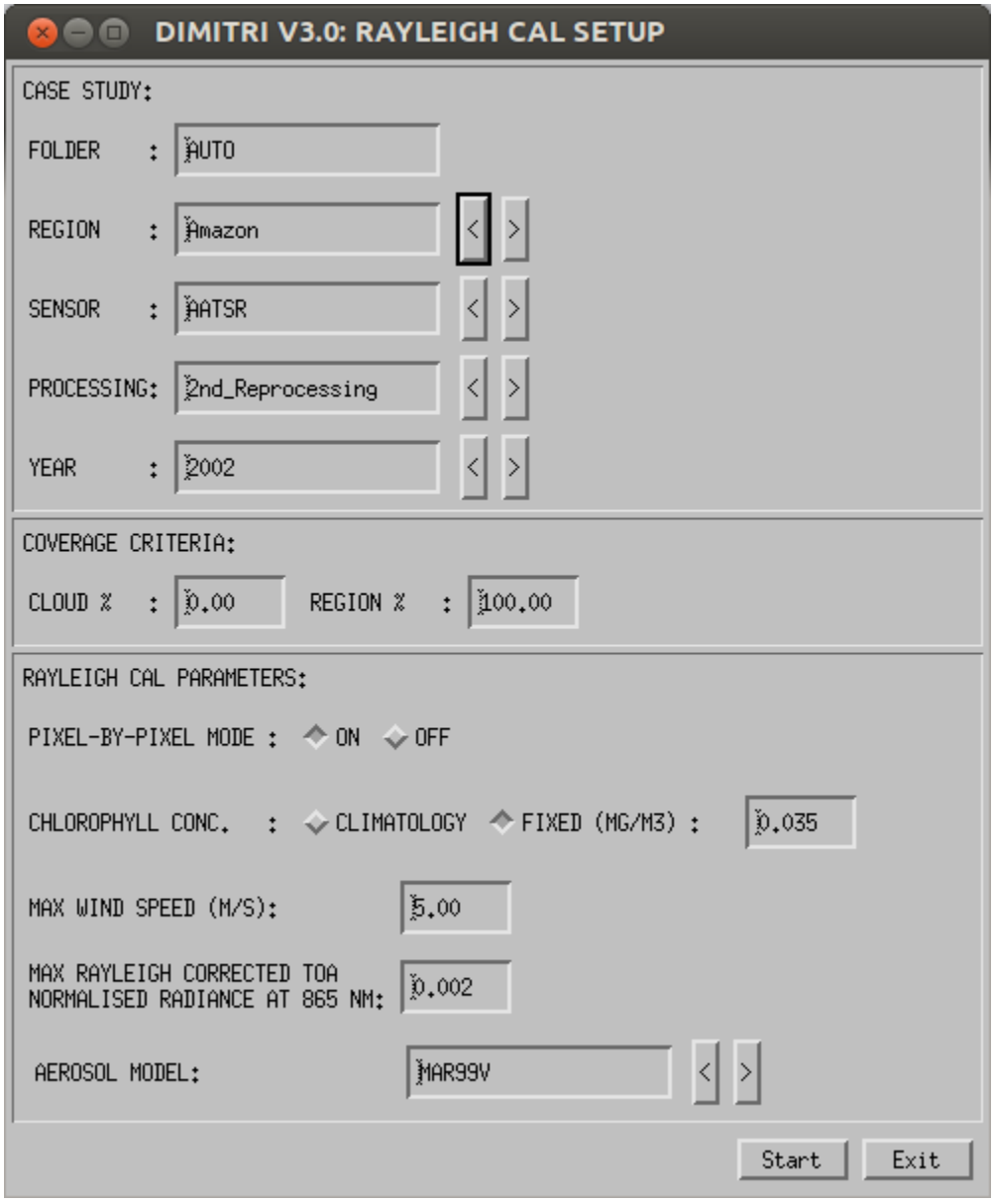

Figure 10: DIMITRI_v3.0 window for parameterising the Rayleigh scattering vicarious calibration

5 Results and implementation comparisons

Note: Wind speed modulus and gas concentrations used for atmospheric quantities computation come from DIMITRI auxiliary data associated to each measurement, as stored in SENSOR_TOA_REF.dat files. Because current DIMITRI version only provides these auxiliary data for MERIS, default values of w_m=5m/s and O_3=300 DU are automatically selected in order to present results for all sensors.

In all the following results default options of the Rayleigh calibration are used, unless otherwise specified:

- Pixel-by-pixel mode
- 0% ROI cloud coverage,
- 100% ROI coverage,
- Maximum wind modulus of 5 m/s,
- Threshold of 0.002 on normalised Rayleigh corrected radiance at 865 nm and
- MAR-99 aerosol model.

Over SPG, chlorophyll concentration comes from previously detailed climatology. Over SIO, which does not provide such data, we follow the initial Hagolle *et al*. (1999) strategy by computing two sets of gains for extreme concentrations (0.035 and 0.17 mg/m^3) and then averaging the gains.

5.1 DIMITRI implementation results for MERIS

The mean coefficients over SPG for MERIS 3rd reprocessing, detailed in Table 10 and plotted against wavelength on Figure 11 present a smooth spectral variation and values from about 4% at 412 nm to 2.6% at 665 nm. However, the standard deviation is quite large, up to 7% in the blue and decreases toward 1.4% in the red. Accordingly, the median give more robust coefficients, with a nearly flat value around 2.2 %. This is close to the estimated 2% error budget of the on-board L1b calibration (Bourg and Delwart, 2012), yet slightly above - we can expect that adding more targets would help drawing a clearer conclusion (only 18 points are available here after data screening).

The time-series (Figure 12) does not show temporal trends, although the few numbers of points does not allow drawing a statistically robust conclusion.

Table 10: MERIS 3rd reprocessing Rayleigh calibration coefficients over SPG

Band (nm)	Median DAk	Mean DAk	Standard deviation	Mean uncertainty	N
412.00	1.022	1.04	0.069	0.042	18
443.00	1.018	1.041	0.066	0.042	18
490.00	1.022	1.029	0.044	0.041	18
510.00	1.025	1.024	0.03	0.041	18
560.00	1.022	1.023	0.021	0.041	18
620.00	1.021	1.023	0.016	0.041	18
665.00	1.026	1.026	0.014	0.041	18

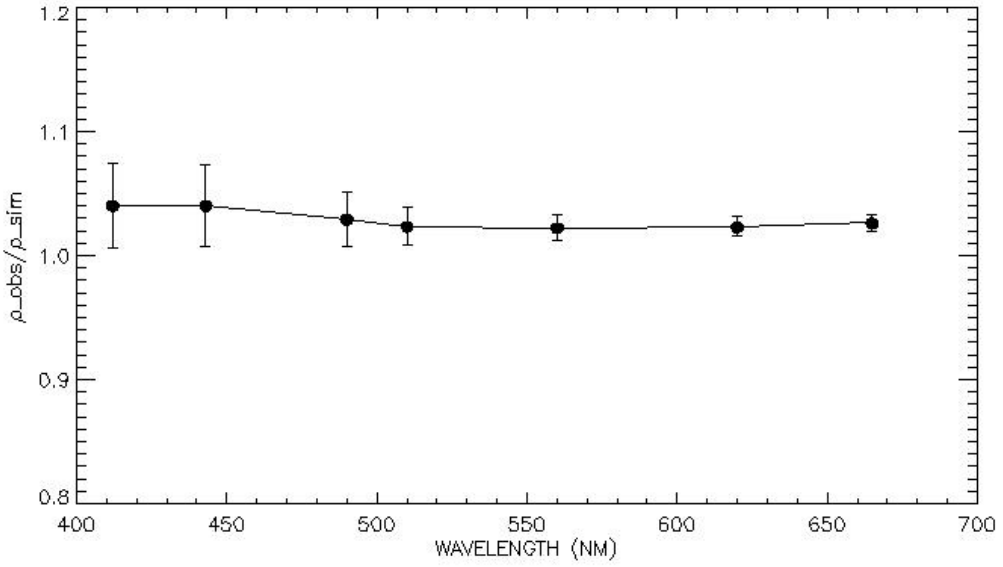

Figure 11 Median MERIS 3rd reprocessing Rayleigh calibration coefficients over SPG as a function of wavelength

At SIO, the two extreme chlorophyll concentrations yield to largely different set of coefficients (Figure 13, top and middle). Clearly this demonstrates the need to properly choose and characterised the calibration site. However combination of both provides realistic vicarious factors, very consistent with previous SPG values (Figure 13, bottom).

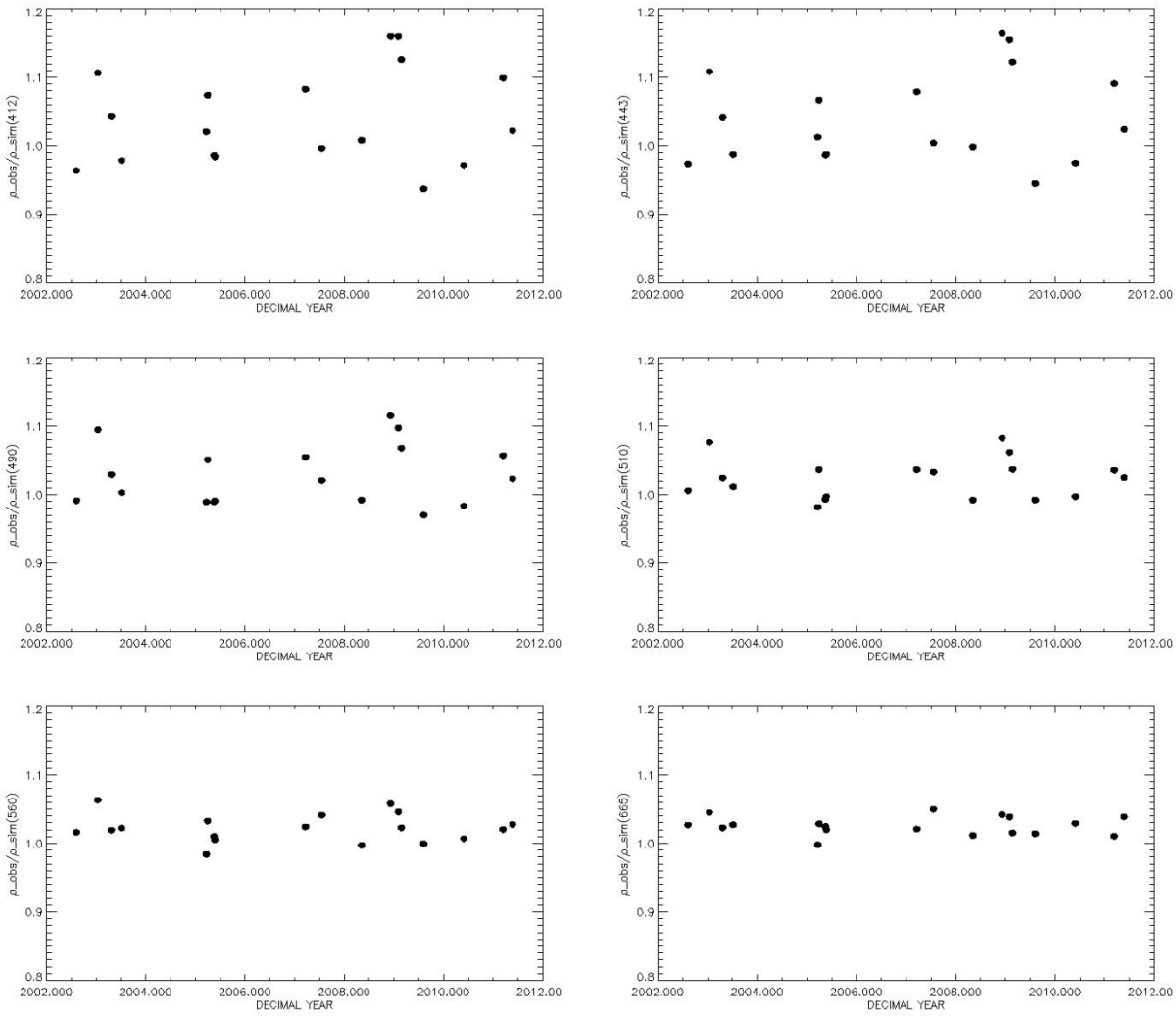

Figure 12: Times series of MERIS 3rd reprocessing Rayleigh vicarious calibration coefficients over SPG at respectively 412, 443, 490, 510, 560 and 665 nm from top to bottom, left to right.

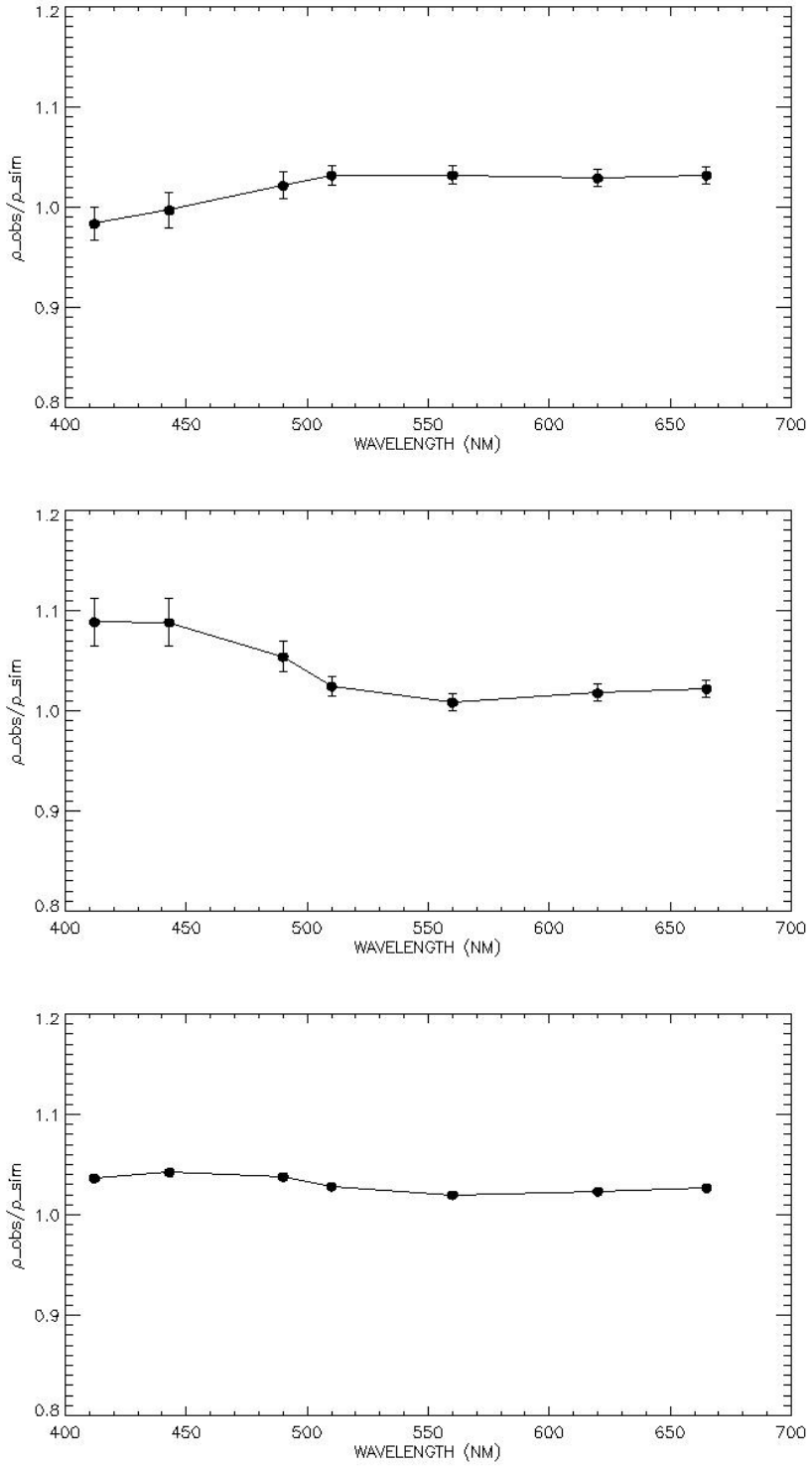

Figure 13: Median MERIS 3rd reprocessing Rayleigh calibration coefficients over SIO for chl=0.035 (top), chl=0.17 mg/m3 (middle) and average of both sets of coefficients (bottom)

Comparison with the nominal vicarious coefficients of MERIS 3rd reprocessing (Lerebourg *et al*. 2011) is shown in Figure 14, in term of vicarious gains g=1/RAk. We first observe an almost constant difference of about -2.7% (at 490 nm, 560 nm, a bit more at 443 nm). Interestingly, shifting the DIMITRI gains to the reference gains at 490 nm allows to retrieve an excellent agreement between the coefficients in term of spectral shape. This is a particularly interesting result since the nominal vicarious calibration differs in two main aspects:

- It first correct the 865 nm band before the bands in the visible;
- Coefficients in the visible are based on in-situ marine reflectance measurement, at other regions (BOUSSOLE and MOBY).

Tests on DIMITRI vicarious coefficients conducted with identical ESA LUTs as in Lerebourg *et al*. (2011) explain that the constant shift is largely due to difference in the RTM LUT (not shown here). A quick way to understand it is to consider the differences between standard ESA LUTs and DIMITRI LUTs generated by Mystic, of about +3% on Rayleigh reflectance at 443 nm for any geometry as shown previously on Figure 5. If we assume this constant 3% difference is true on the path signal and that the TOA marine signal represent about 15% of the total signal for very clear waters (see Figure 1 in Lerebourg *et al*. 2011), then the difference on the vicarious gains due to difference in path reflectance is of:

$$\frac{\Delta g}{g} = \frac{0.85}{1.03} 0.15 - 1 \approx -2.5\%$$

This estimate corresponds very well to the observed constant shift between both approaches.

Eventually, we observe that the standard deviation of coefficients is between two and five time bigger for the Rayleigh calibration; we recall here that DIMITRI results are based on only 18 points, against about 100 for MERIS 3rd reprocessing vicarious calibration.

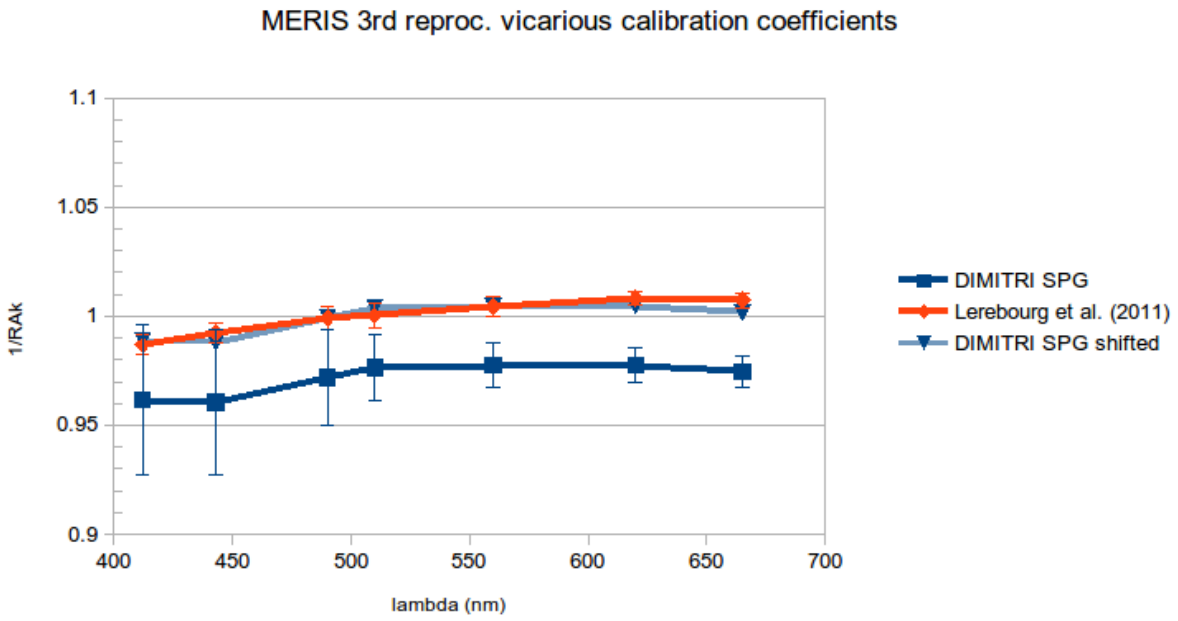

Figure 14: MERIS 3rd reprocessing mean gains (expressed in term of 1/RAk) as of DIMITRI Rayleigh calibration over SPG (dark blue) and for nominal MERIS vicarious calibration (red, from Lerebourg et al. 2011). Clear blue ligne represents DIMITRI gains shifted on the nominal gain at 490 nm

Regarding MERIS 2nd reprocessing, same order of vicarious coefficients are found, of about 2% but without a bump near the blue (see for SPG). This systematic bias is not present in CNES computation of Fougnie *et al*. (2012), possibly again because this latter approach consider at least six oceanic regions and different RTM LUTs.

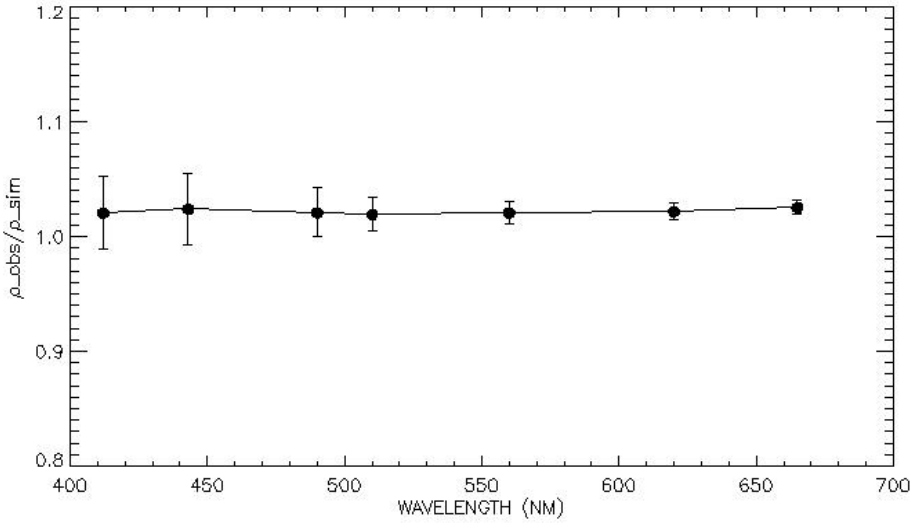

Figure 15: DIMITRI Rayleigh vicarious coefficients at SPG for MERIS 2nd reprocessing

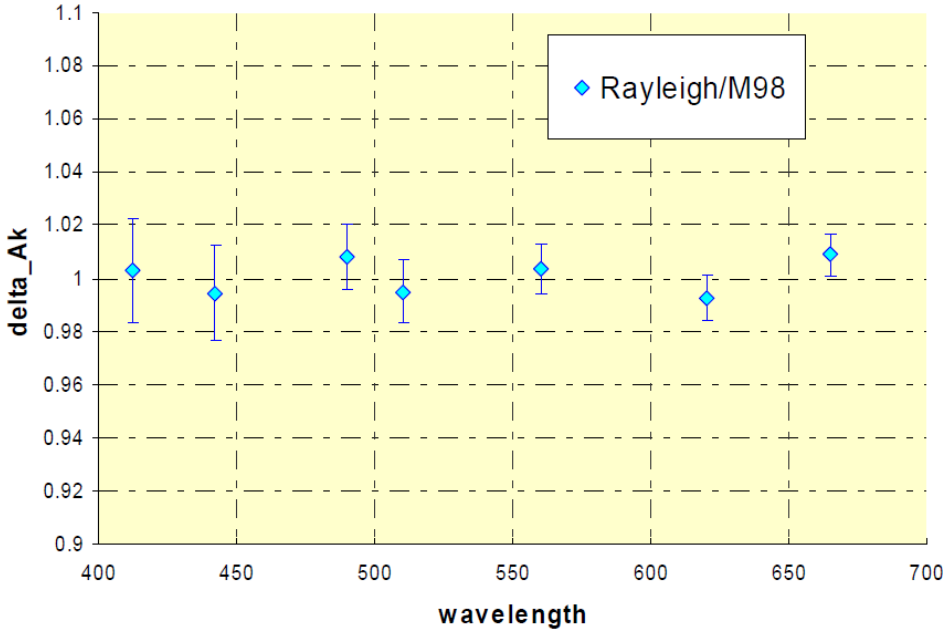

Figure 16: CNES Rayleigh vicarious calibration coefficients for MERIS 2nd reprocessing. From Fougnie et al 2012.

5.2 Preliminary DIMITRI implementation results for other sensors

Rayleigh calibration coefficients over SPG for MODISA, PARASOL, AATSR and ATSR2 are displayed on Figure 17 to Figure 20. Since VEGETATION does not image this oceanic region, we present calibration over the BOUSSOLE site on Figure 21, based on chlorophyll climatology provided by ESA through GlobColour archive (Bouvet 2013). We remind here that the meteorological auxiliary data do not currently exist for these sensors, hence following results should be considered as preliminary.

MODISA coefficients remain close to unity, within 2%, except at 666 nm. PARASOL coefficients present a consistent spectral shape with Fougnie *et al*. (2007), with however a large positive shift of about 5% in the blue/green; comparison is however very limited due to difference in calibration sites and the time range (3 months in 2005 over 6 oceanic sites in Fougnie et al (2007), this latter emphasizing also a temporal drift thanks to other calibration methods).

PARASOL, AATSR and AATSR2 presents larger standard-deviations, which is possibly due to the averaging multi-directional views in single observations.

VEGETATION coefficients at BOUSSOLE show a perfect calibration at 645 nm while a 0.95 factor is found at 450 nm. Note however that only 6 points were selected because only ROI averaged extractions are currently available in DIMITRI database.

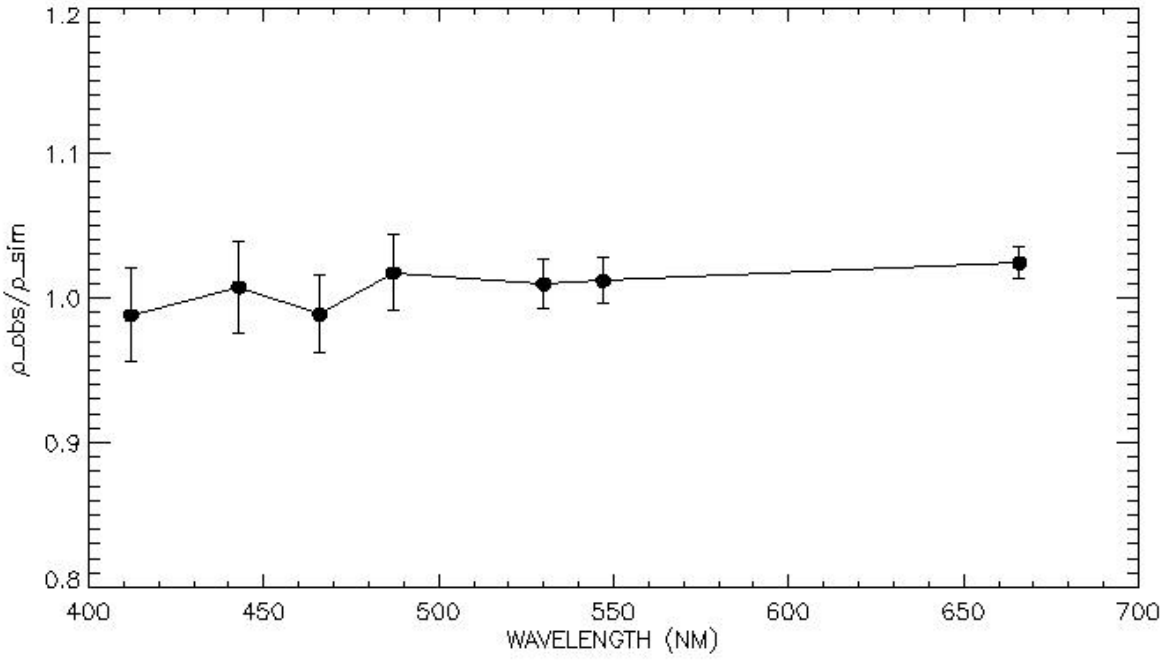

Figure 17: MODIS Rayleigh calibration coefficients over SPG.

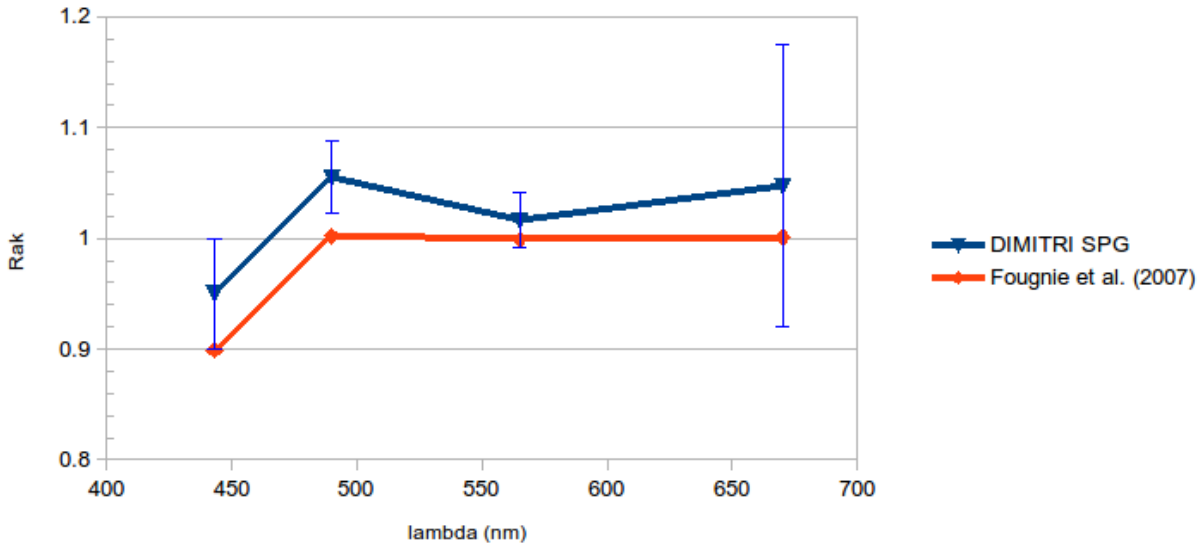

Figure 18: PARASOL Rayleigh calibration coefficients over SPG for DIMITRI (blue) and from Fougnie et al (2007) (red).

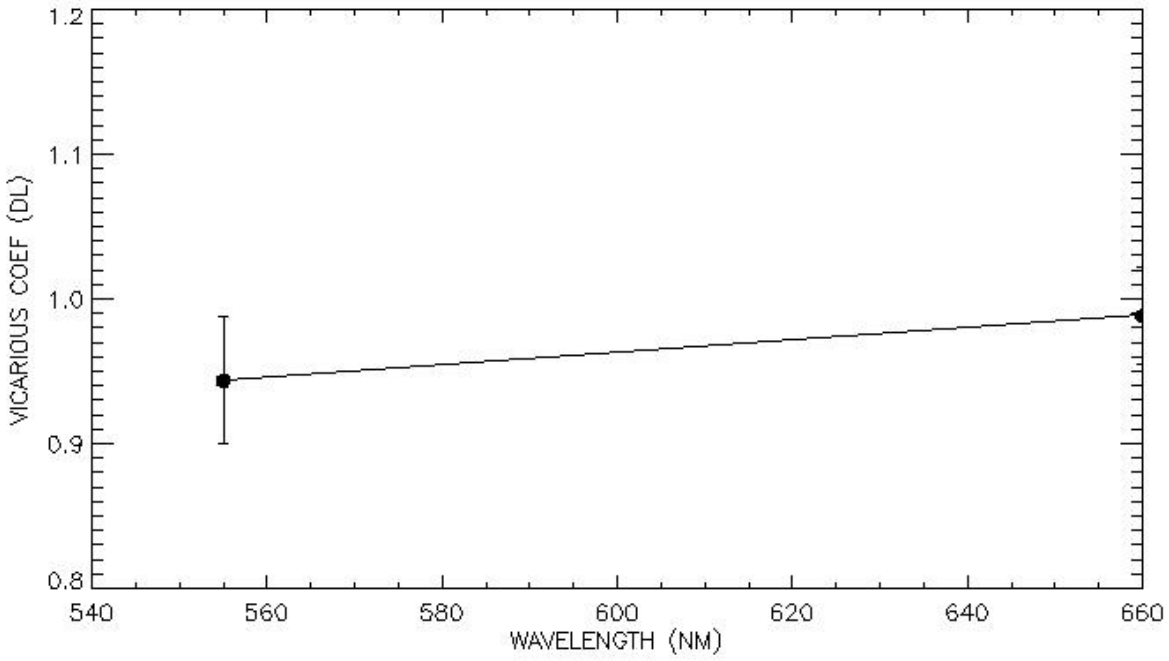

Figure 19: AATSR Rayleigh calibration coefficients over SPG.

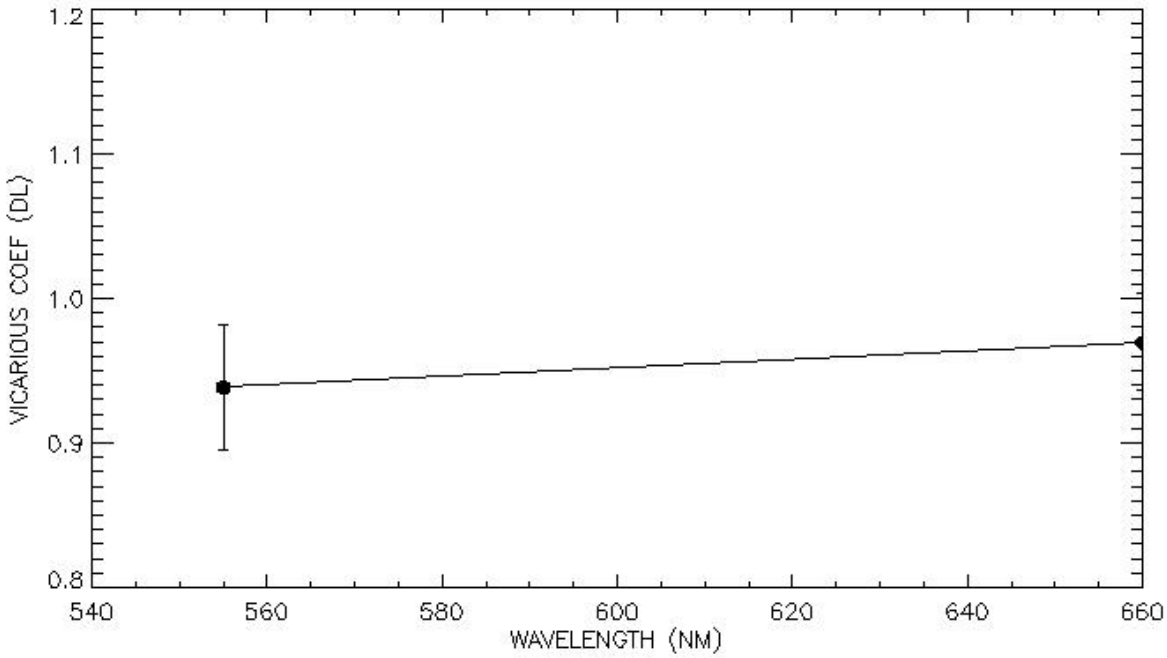

Figure 20: ATSR2 Rayleigh calibration coefficients over SPG.

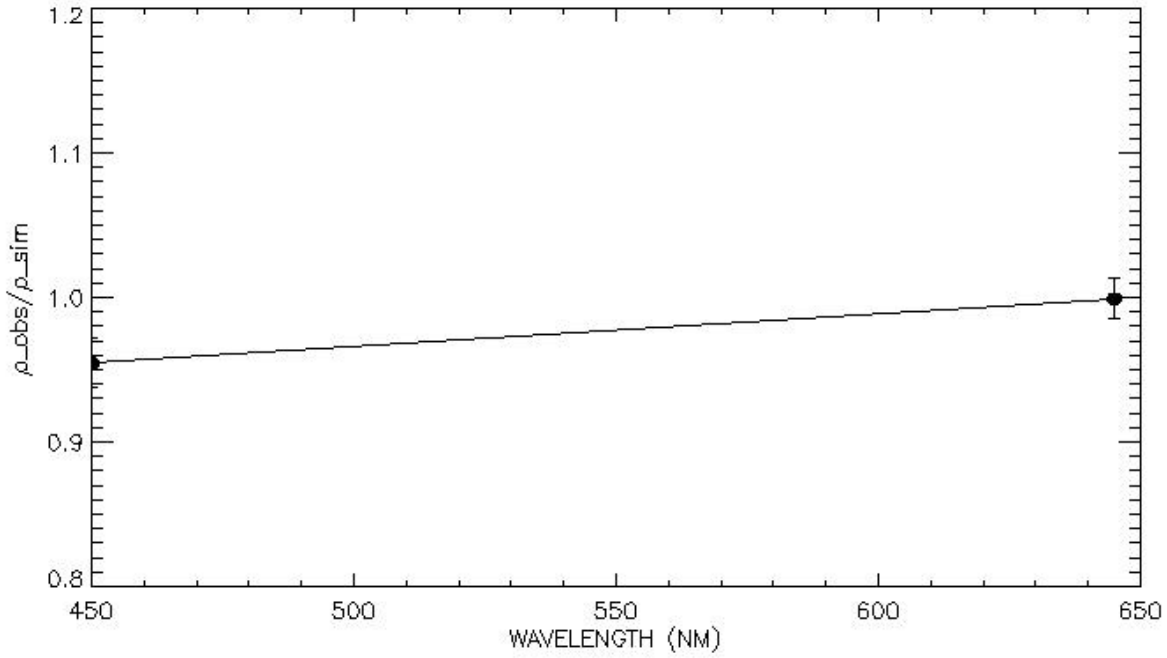

Figure 21 VEGETATION Rayleigh calibration coefficients over BOUSSOLE.

6 Discussion and conclusion

The Rayleigh calibration method implemented in DIMITRI_v3.0 follows essentially the initial work of Hagolle *et al*. (1999), with several adaptations taking into account more recent and well-tried ocean colour modelling in marine reflectance and aerosol contribution.

The DIMITRI_v3.0 HMI allows users to easily choose all main parameters of the calibration (thresholds, chlorophyll concentration, aerosol model, etc.). Automated handling of auxiliary files also gives users the possibility to immediately test other parameterisations of the signal modelling, both for the marine contribution (e.g. chlorophyll climatology, coefficients of the Morel and Maritorena (2011) model) and atmospheric component (e.g. new look-up tables with different geometrical discretisation or aerosol models).

Vicarious coefficients presented here for MERIS are in good agreement with other published approaches in term of spectral shape (Lerebourg *et al*., 2011) but at the limit of the expected L1b calibration uncertainty of 2% (Bourg and Delwart, 2012). We have seen that a constant shift in calibration coefficients could be due to systematic difference in RTM LUT (in particular Rayleigh); hence a deeper comparison between different set of RTM LUTs is of much interest, yet out of the scope of present ATBD. DIMITRI v3.0 provides through the stored SAV files all necessary data for further exploiting the methodology.

Results and analysis have shown the necessity to increase the number of calibration points as well as to perfectly characterize their chlorophyll concentration. In particular, the DIMITRI SIO site is not optimal because of high concentration and seasonal change. We recommend enriching the DIMITRI database with oceanic targets studied in Fougnie *et al*. (2002) and used in Fougnie *et al*. (2012).

In order to get finalised coefficients of all sensors, we recommend running the Rayleigh calibration with meteorological auxiliary data for AATSR, ATSR2, MODIS, PARASOL and VEGETATION.

7 References

Antoine, D. and A. Morel (1999). A multiple scattering algorithm for atmospheric correction of remotely-sensed ocean colour (MERIS instrument): principle and implementation for atmospheres carrying various aerosols including absorbing ones, IJRS, 20, 1875-1916.

Antoine, D. and Morel, A. (2011). MERIS ATBD 2.7 Atmospheric Correction of the MERIS observations Over Ocean Case 1 waters. Technical Report MERIS ATBD 2.7 v5.1-July2011 (Version 5.1).

Barker, K., Antoine, D., Bourg, L., Brockmann, C., Doerffer, R., Fischer, J., Moore, G., Santer, R., and Zagolski, F. (2012). Reference Model for MERIS Level 2 Processing. Third MERIS reprocessing: Ocean Branch. Technical Report PO-TN-MEL-GS-0026 (Version 5.2)

Bourg, L. and S. Delwart (2012) MERIS instrument calibration. Available at http://earth.eo.esa.int/pcs/envisat/meris/documentation/

Bouvet, M. (2006). Intercomparisons of imaging spectrometers over the Salar de Uyuni (Bolivia). *Proc. 2nd MERIS and AATSR Calibration and Geophysical Validation Meeting (MAVT-2006)*, 20-24 March 2006, ESRIN.

Bouvet, M. (2011). Simulation of VEGETATION measurements with DIMITRI. ESA Tech. Note: TEC-EEP/2011.713/MB

Bouvet, M. (2013) Selection of optimum oceanic sites for applying the Rayleigh scattering methodology to optical space sensors. ESA Technical Note, 06/12/2013.

Bouvet M., Goryl P., Chander G. Santer R., and Saunier S. (2007). Preliminary radiometric calibration assessment of ALOS AVNIR-2. Proc. Geoscience and Remote Sensing Symposium, IGARSS 2007

Cox, C., and W. Munk (1954), Statistics Of The Sea Surface Derived From Sun Glitter, J. Mar. Res., 13, 198 – 227

Fougnie, B., Patrice Henry, P., Morel, A., Antoine, D., Montagner, F. (2002). Identification and characterization of stable homogenous oceanic zones: climatology and impact on in-flight calibration of space sensors over rayleigh scattering. Ocean Optics XVI, Santa Fe, NM.

Fougnie, B., Bracco, G., Lafrance, B., Ruffel, C., Hagolle, O., Tinel, C. (2007) PARASOL in-flight calibration and performance, Applied Optics, Vol. 46, No 22, 5435-5451

Fougnie, B., Henry, P., Lachérade, S., and P. Gamet (2012) Radiometric calibration of desert sites and oceanic target. Sentienl-3 calibration and validation planning meeting, ESA/ESRIN, March 2012.

Hagolle *et al*. (1999) Results of POLDER in-flight Calibration, IEEE Transactions on Geoscience and Remote Sensing, May 1999, Volume 37, Number 03

Hansen, J.E. and L. Travis, 1974. Light scattering in planetary atmospheres, Space Science Reviews,

16: 527-610.

Hedley J, Lamquin N, Mazeran C. (2013) Atmoshperic Correction for Ocean Colour in a Spherical Shell Atmosphere. Algorithm Theoretical Basis Document. ESA Report GEOHR-D6 AO/1-7084/12/NL/AF (Version 0.9.2).

Hess M, Koepke P, Schult I (1998) Optical Properties of Aerosols and Clouds: The software package OPAC. Bulletin of the American Meteorological Society 79(5) 831-844.

Kay, S., Hedley, J., Lavender, S., and Nimmo-Smith, A. (2011). Light transfer at the ocean surfacemodelled using high resolution sea surface realizations. Opt. Express, 19(7):6493–6504.

Kou, L., D. Labrie, P. Chylek, 1993, "Refractive indices of water and ice in the 0.65-2.5 m spectral range," Appl. Opt.,32, 3531-3540 (1993).

Kujanpää, J. (2013). Atmospheric Correction for Geostationary High Resolution Ocean Applications (GEO-HR). Forward Model Description. Technical Report ESA Report GEOHR-D2 AO/1-7084/12/NL/AF (Version 1.1).

Lerebourg, C., Mazeran, C., Huot, J-P., Antoine, A. (2011) Vicarious adjustment of the MERIS Ocean Colour Radiometry. MERIS ATBD 2.24, Issue 1.0

Mayer, B. (2009). Radiative transfer in the cloudy atmosphere. EPJ Web of Conferences, 1:75–99.

Mayer, B. and Kylling, A. (2005). Technical note: The libradtran software package for radiative transfer calculations - description and examples of use. Atmospheric Chemistry and Physics, 7:1855–1877.

MERIS Level 2 Detailed Processing Model, June 2011, ref. PO-TN-MEL-GS-0006, Issue 8.0B available at http://earth.eo.esa.int/pcs/envisat/meris/documentation

Morel, A. (1988). Optical modeling of the upper ocean in relation to its biogenous matter content (case 1 water), Journal of Geophysical Research, 93, 10,749-10,768.

Morel, A., and S. Maritorena (2001). Bio-optical properties of oceanic waters: A reappraisal. Journal of Geophysical research, 106, 7763-7780

Morel, A., and B. Gentili (1996). Diffuse reflectance of oceanic waters. 3. Implication of bidirectionality for the remote-sensing problem. Applied Optics, 35, 4850-4862.

Morel, A. and Gentili, B. (1993). Diffuse reflectance of oceanic waters. ii bidirectional aspects.Applied Optics, 32(33):6864–6879.

Morel, A., Gentili, B., Chami, M., and J. Ras (2006) Bio-optical properties of high chlorophyll Case1 waters and of yellow-substance-dominated Case2 waters. Deep-Sea Res. I, 53, 1439-1559

Pope, R. M. and E. S. Fry, 1997, "Absorption spectrum (380-700 nm) of pure water. II. Integrating cavity measurements," Appl. Opt.,36, 8710-8723.

Shettle, E.P. and R.W. Fenn, 1979. Models for the aerosols of the lower atmosphere and the

effects of humidity variations on their optical properties. Environmental Research Papers, AFGL-TR-79-0214, 20 September 1979, AFGL, Hanscom (Mass.).

Smith, R.C. and K.S. Baker, 1981, "Optical properties of the clearest natural waters (200-800 nm)," Appl. Opt.,20, 177-184.

Vermote, E., R. Santer, P.Y. Deschamps and M. Herman, In-flight Calibration of Large Field-of-View Sensors at Short Wavelengths using Rayleigh Scattering, Int. Journal of Remote Sensing, 13, No 18, 1992. http://www.tandf.co.uk/journals/tres

Yang, H. and Gordon, H. R. (1997). Remote sensing of ocean color: assessment of water-leaving radiance bidirectional effects on atmospheric diffuse transmittance. Applied Optics, 36(30):7887–7897.

Zagolski, F. (2010) Specification of the Contents of the MERIS Radiative Transfer Tools used to Generate the Level-2 Auxiliary Data Products. Doc PO-RS-PAR-GS-0003, issue 4.A

[End of Document]